This version represents the manuscript that was resubmitted to *Geochemistry, Geophysics, Geosystems* following peer-review on August 4th 2021.

Insights into the nature of plume-ridge interaction and outflux of H_2O from the Galápagos Spreading Centre

Matthew L. M. Gleeson[1,2*] and Sally A. Gibson[1]

[1]Deparment of Earth Sciences, University of Cambridge, Downing Street, Cambridge, UK, CB2 3EQ.

[2]School of Earth and Environmental Sciences, Cardiff University, Park Place, Cardiff, CF10 3AT, UK

Corresponding author email: gleesonm1@cardiff.ac.uk

KEY POINTS

1. Basalts erupted on segments of the global ridge system adjacent to the Galapagos mantle plume have high volatile (H_2O & F) contents.
2. Channelised melt transport between the Galápagos mantle plume stem and the GSC causes variations in crustal thickness and geochemistry.
3. Plume-derived volatile-rich melts contribute up to 20 – 60% of the total H_2O outflux at the Galápagos Spreading Centre.

This version represents the manuscript that was resubmitted to *Geochemistry, Geophysics, Geosystems* following peer-review on August 4th 2021.

ABSTRACT

The flow of high-temperature and compositionally-enriched material between mantle plumes and nearby spreading centres influences up to 30% of the global mid-ocean ridge system and represents a significant, but currently unconstrained, flux of volatiles out of the mantle. Here we present new analyses of H_2O, F, Cl and S in basaltic glass chips from an archetypal region of plume-ridge interaction, the Galápagos Spreading Centre (GSC). Our dataset includes samples from the eastern GSC, on ridge segments that are strongly influenced by the adjacent Galápagos mantle plume, and complements published analyses of volatiles largely from the western GSC. We use forward models of mantle melting to investigate the role of solid and melt-phase transport from a lithologically heterogeneous (peridotite-pyroxenite) mantle in plume-ridge interaction along approximately 1000 km of the GSC. Our results indicate that the observed geochemical and geophysical variations cannot be recreated by models which only involve solid-state transfer of material between the Galápagos mantle plume and the GSC. Instead, we show that the geochemical and geophysical data from the GSC are well-matched by models that incorporate channelised flow of volatile-rich melts formed at high-pressures (>3 - 4 GPa) in the Galápagos plume stem to the GSC. In addition, our new models demonstrate that channelised flow of enriched, plume-derived melt can account for up to ~60% of the H_2O outgassed from regions of the GSC which are most strongly influenced by the Galápagos mantle plume.

PLAIN LANGUAGE SUMMARY

Approximately one-third of Earth's global mid-ocean ridge system is influenced by the transfer of compositionally distinct material from nearby upwellings of anomalously hot mantle. Transfer of this plume material to oceanic spreading centres might represent an important mechanism of volatile loss from Earth's mantle, but there are limited constraints on the quantities of H_2O and other

volatiles that degas from these plume-influenced spreading centres. In this study, we evaluate the mechanism of plume-ridge interaction between the Galápagos mantle plume and the nearby Galápagos Spreading Centre (GSC) using new analyses of volatiles in basalts erupted on the ridge. The results from new numerical models demonstrate that the geochemical and geophysical signatures of plume-ridge interaction along the GSC are best explained if the transport of deep sourced mantle material between the Galápagos mantle plume and GSC occurs in the melt phase rather than as a solid. In addition, our new analyses enable us to constrain the flux of H_2O out of the GSC and demonstrate that melt channelization can account for up to ~60% of the H_2O flux out of plume-influenced ridges.

1 INTRODUCTION

The majority of ocean island basalts (OIBs) are believed to form as a consequence of adiabatic decompression melting in high-temperature, and potentially lithologically-heterogeneous, mantle plumes (Asimow and Langmuir, 2003; Herzberg and Asimow, 2008; Ito and Mahoney, 2005; Métrich et al., 2014; Morgan, 1971; Sobolev et al., 2007). Higher concentrations of volatiles (such as H_2O, F, or Cl) in OIBs compared to mid-ocean ridge basalts (MORBs) reflect the volatile-rich nature of deep-sourced plume material, relative to the MORB source, and are evidence of small-fraction decompression melting at higher pressures than the anhydrous peridotite solidus (Dixon et al., 2017; Gibson and Richards, 2018; Ingle et al., 2010; Jackson et al., 2015; Koleszar et al., 2009; Métrich et al., 2014). In addition, approximately 30% of the global mid-ocean ridge (MOR) system is influenced by the lateral transfer of deep-sourced mantle plume material (Ito and Lin, 1995) and potentially represent sites of substantial volatile outgassing from the Earth's mantle (Gibson and Richards, 2018; Le Voyer et al., 2018). Nevertheless, robust estimates for the outflux of volatiles from mantle plume influenced segments of MORs are rare. In addition, there remain outstanding issues related to

the role of melt channelisation in the transfer of geochemically enriched plume material between mantle plume stems and nearby spreading centres.

Over the past few decades, numerous hypotheses have been put forward to explain both the long and short length-scale geochemical and geophysical heterogeneities that are observed along plume-influenced regions of the global MOR system. These previously proposed hypotheses include: (i) buoyancy-driven upwelling of solid peridotite beneath ridge segments that are most strongly influenced by nearby mantle plumes (e.g. Ingle et al., 2010; Maclennan et al., 2001; Sleep, 1990); (ii) radial spreading of solid plume material, consisting of enriched blebs embedded in a depleted matrix (and the role of these enriched components in dynamic plume flow; Bianco et al., 2013; Ito and Bianco, 2014; Ito and Mahoney, 2005; Ribe, 1996; Shorttle et al., 2010); (iii) flow of solid plume material in a sub-lithospheric channel (Morgan, 1978; Schilling et al., 1982); (iv) melt transport via porous flow at the base of the lithosphere (Braun and Sohn, 2003); and (v) channelized gravitational flow of off-axis plume-derived melts in a matrix of dispersing solid plume material (Gibson et al., 2015; Gibson and Richards, 2018; Mittal and Richards, 2017; Stroncik et al., 2008; Stroncik and Devey, 2011).

Channelised, gravitational flow of volatile-rich melts in a network of channels embedded in a spreading 'puddle' of solid plume material (hypothesis (v) above) was first put forward by Gibson et al. (2015) to account for the simultaneous presence of enriched basalts on the GSC and depleted basalts found in nearby regions of the northeast Galápagos Archipelago (e.g. Genovesa). Subsequently, Mittal and Richards (2017) and Gibson and Richards (2018) extended this conceptual model to account for certain enigmatic features at global sites of plume-ridge interaction (including the GSC), such as the coincidence of the intersection of non-age progressive volcanic lineaments with excess crustal thickness and short length-scale geochemical anomalies (i.e. highly-enriched basalts) on the spreading ridge.

Despite continued development in the conceptual models of plume-ridge interaction via a network of melt channels embedded in solid plume material, a focused geochemical study on the role of channelised volatile-rich melts to an individual spreading centre has yet to be undertaken. Here, we present new volatile data (H_2O, F, Cl and S) for basaltic glass chips from plume-influenced segments of the GSC, including the eastern GSC where only limited volatile data previously existed (e.g. Byers et al., 1983). We use our new and published volatile data in combination with forward melting models to evaluate whether plume-ridge interaction via channelised flow of volatile-rich melts derived from a pyroxenitic source component in a mixed peridotite-pyroxenite mantle is able to explain the long (100s of km) and short (10s of km) length-scale heterogeneities observed in basalt chemistry and crustal thickness at this single site of plume-ridge interaction. Our new volatile data and forward models of mantle melting also allow us to estimate the outflux of H_2O from the entire region of Galápagos plume-influenced ridge.

2 GEOLOGICAL BACKGROUND

2.1 MANTLE HETEROGENEITY

Located ~1000 km off the western coast of Ecuador, the Galápagos Archipelago represents a well-known example of mantle plume related volcanism (Morgan, 1978). Active and recent Holocene volcanism is observed over a wide geographic area and geochemical studies of both subaerial and submarine basaltic lavas reveal that compositional heterogeneity results from the melting of at least 4 isotopically-distinct components in the Galápagos mantle plume (Geist et al., 1998; Harpp and Weis, 2020; Harpp and White, 2001; Hoernle et al., 2000; White and Hofmann, 1978; White et al., 1993). The isotopic end-members of the Galápagos mantle plume include an isotopically depleted component and 3 isotopically enriched mantle components, that can be summarised as:

1. PLUME component - dominant in basalts from the western Galápagos Archipelago (centred on Isla Fernandina), which are characterised by moderately enriched Sr, Nd and Pb isotope

ratios and elevated $^{3}He/^{4}He$ ratios (~30 R/R_A; Harpp and White, 2001; Kurz et al., 2009; Kurz and Geist, 1999). The isotopic signatures of the PLUME component resembles the 'FOZO' or 'C' global mantle end-member (Hanan and Graham, 1996; Hart et al., 1992).

2. Floreana (FLO) component – centred on the southern island of Floreana and characterised by the most radiogenic Sr and Pb isotope signatures observed anywhere in the Galápagos (Harpp et al., 2014a; Harpp and White, 2001). The FLO component is hypothesised to result from melting of ancient recycled oceanic crust (~2.2 – 2.5 Ga) incorporated into the Galápagos plume (Gibson et al., 2016; Harpp et al., 2014).

3. Wolf-Darwin (WD) component – most prevalent in basaltic lavas from the northern islands of Pinta, Wolf, Darwin and surrounding seamounts (Harpp et al., 2014c; Harpp and White, 2001). The WD component is characterised by elevated $^{208}Pb/^{206}Pb$ and $^{207}Pb/^{206}Pb$ ratios (Harpp and White, 2001). The origin of this component remains enigmatic.

The spatial heterogeneity in the radiogenic isotope composition of basalts erupted in the Galápagos Archipelago provides insights into the structure of the underlying plume and the deep mantle. For example, isotopically enriched signatures are most commonly observed in the south-western Archipelago (corresponding to the PLUME and FLO components), whereas isotopically depleted basalts are typically found further east (Harpp and Weis, 2020; Harpp and White, 2001; Hoernle et al. 2000; White and Hofmann, 1978; White et al., 1993). This bilateral asymmetry in the composition of the upwelling mantle plume, which is similar to that observed in Hawaii and other regions of plume-derived volcanism worldwide (Harpp et al., 2014b; Weis et al., 2011), has been linked to the presence of deep mantle superstructures at the base of the Galápagos plume (Harpp and Weis, 2020; Gleeson et al. 2021). Specifically, the isotopically-enriched signatures of the south-western Galápagos have been assigned to melting of material originating in the Pacific Large Low Shear Velocity Province, whilst the isotopically-depleted signatures of the eastern Galápagos volcanoes are assigned to melting of the ambient Pacific lower mantle or entrained upper mantle material (Harpp

and Weis, 2020). This simple picture of mantle isotopic heterogeneity in the Galápagos plume is complicated by the non-trivial relationship between isotopic and lithological heterogeneity. Olivine minor element concentrations were originally used to indicate that both isotopically-enriched and isotopically-depleted pyroxenite components are present in the Galápagos mantle plume (Vidito et al., 2013). However, recent models that consider the influence of magma chamber recharge on the minor element contents of magmatic olivines suggest that basalts sourced from the isotopically-depleted mantle component in the Galápagos are predominantly derived from a peridotitic source (Gleeson and Gibson, 2019). Nevertheless, variations in the Fe-isotope composition of the GSC basalts indicate that both peridotite and pyroxenite source components might contribute to the composition of plume-influenced basalts on the GSC (Gleeson et al., 2020).

2.2 Geophysical and Geochemical Heterogeneity along the GSC

The Galápagos Spreading Centre separates the Cocos and Nazca tectonic plates and lies ~150-250 km north of the centre of Galápagos plume upwelling, at 100 km depth, that has been postulated from seismic tomography (Fig. 1; Hooft et al., 2003; Villagómez et al., 2014). This lies to the north-east of the postulated location of the plume stem at 200 km depth, i.e. beneath southern Isabela. Variations in crustal thickness and ridge morphology provide evidence for the influence of the Galápagos mantle plume along a ~1000 km wide zone of the GSC, extending between 85.5°W and 95.5°W (e.g. Christie et al., 2005; Ito and Lin, 1995). For example, a crustal thickness high is observed at ~90.5 °W, near the closest point on the GSC to the centre of the mantle plume upwelling (Canales et al., 2002; Christie et al., 2005; Detrick et al., 2002; Mittelstaedt et al., 2014).

Several features observed along both the eastern and western GSC, which are separated by a major transform fault at ~91°W (the Galápagos Transform fault - GTF; Fig. 1), are consistent with a decrease in magma supply with increasing distance from the mantle plume (Canales et al., 2014). For example, changes in ridge morphology, from a low-relief valley and ridge terrain to a prominent axial ridge, are observed on both ridge segments as the separation distance between the ridge and

hotspot decreases (Christie et al., 2005; Sinton et al., 2003). Additionally, along the western GSC the depth of the seismically-imaged magma lens increases from 1-2.5 km east of 92.5°W to 2.5-4.5 km between 92.7°W and 94.7°W, corresponding to a change from fissure-fed eruptions near the GTF to point source eruptions further west (Behn et al., 2004; Blacic et al., 2004).

A prominent geochemical anomaly has been observed on the GSC near the GTF, between 89.5°W and 92.5°W (Christie et al., 2005; Ingle et al., 2010; Schilling et al., 2003). Basalts erupted within this region are characterised by elevated concentrations of strongly incompatible trace elements (e.g. Nb, La) together with radiogenic Sr and Pb and unradiogenic Nd and Hf isotope ratios (Christie et al., 2005; Gleeson et al., 2020; Ingle et al., 2010; Schilling et al., 2003, 1982). Many incompatible trace element ratios (such as Sm/Yb and Nb/Zr) display broadly symmetric profiles that are centred around ~91 – 91.5 °W, just to the west of the GTF (Fig. 1). In addition, positive correlations between the large variations in incompatible trace element enrichment and Fe-isotopes in the GSC basalts imply that the plume-influenced GSC basalts may be formed through melting of a lithologically-heterogeneous mantle source (Gleeson et al., 2020).

Some important differences exist between the eastern and the western GSC. Firstly, the highest resolution gravity and multi-beam bathymetry data available indicates that crustal thickness increases by ~1 km from west to east across the GTF (Mittelstaedt et al., 2014). Secondly, the eastern GSC basalts generally have lower ratios of fluid-mobile to fluid-immobile trace elements (e.g. Ba/Nb; Fig. 1) and lower $^{208}Pb/^{204}Pb$ and $^{207}Pb/^{204}Pb$ ratios than basalts from the western GSC (e.g. Christie et al., 2005; Gibson et al., 2015; Ingle et al., 2010; Schilling et al., 2003). The long length-scale east-to-west geochemical differences on the GSC have been attributed to an additional contribution of melts from the isotopically-enriched Wolf-Darwin Galápagos mantle component beneath the western GSC (Gibson et al., 2015; Ingle et al., 2010; Schilling et al., 2003).

Gibson and Richards (2018) observed a series of short length-scale geochemical and geophysical features that are superimposed on the broad length-scale heterogeneity of the GSC. For example,

basalts with anomalously high H_2O contents relative to their neighbouring basalts (typically >0.4 wt.%), and short length-scale crustal thickness anomalies occur at locations where long-lived volcanic lineaments intersect the GSC (Mittelstaedt et al., 2014; Sinton et al., 2003). As a result, it has been suggested that melt channels embedded within the 'normal' spreading of Galápagos plume material may represent an important component of plume-ridge interaction (Gibson and Richards, 2018; Mittal and Richards, 2017). In this study, we use new melting models to critically evaluate the role of both a mixed peridotite-pyroxenite mantle and melt channelisation from the Galápagos plume stem in generating short and long length-scale geochemical and geophysical heterogeneities on the GSC. In addition, our new data expands the existing volatile dataset for the GSC and enables us to place improved constraints on the flux of H_2O out of the entire segment of plume-influenced ridge.

3 METHODOLOGY

Twenty-two chips of basaltic glass (1-10 mm diameter) collected between 83 and 98°W on the Galápagos Spreading Centre were selected from the Jean-Guy Schilling collection at the University of Rhode Island, USA. Here we present new analyses of their H_2O, F, Cl, and S concentrations (Fig. 1). The major and trace element contents of the selected glasses, together with their Fe, Sr, Nd, Hf, and Pb isotope ratios, have previously been reported (Schilling et al., 2003; Gleeson et al., 2020). We primarily selected samples from the eastern GSC for this analysis, as only limited volatile data previously existed in this region, but a small number of samples (n=6) were chosen from the western GSC to check that our results are consistent with previous studies (e.g., Cushman et al. 2004; Ingle et al., 2010).

Basaltic glass chips in polished epoxy mounts were analysed for sulfur on a Cameca SX100 EPMA in the Department of Earth Sciences at the University of Cambridge. Sulfur was analysed alongside major elements (following methods described in Gleeson et al., 2020) to calculate the required

matrix correction. The S concentrations were determined by counting for 90 s on the K_a peak using a beam current of 10 nA, an acceleration voltage of 15 kV, and a defocussed beam (10 µm). Data quality was checked using the VG2 basaltic glass standard (Jarosewich et al., 1980).

Prior to analysis of H_2O, F, and Cl on a Cameca ims-4f at the NERC Edinburgh Ion Microprobe Facility (EIMF), the GSC glasses were briefly re-ground and polished, to remove topography caused by prior laser ablation analysis, and gold coated. Secondary Ion Mass Spectrometry (SIMS) analysis was carried out using a $^{16}O^-$ primary ion beam and a 14.5 keV net impact energy (4.5 keV secondary ion accelerating voltage). A liquid nitrogen cold trap was used to reduce background counts on volatile elements during analysis. Both static and electrostatic magnets were applied to centre H^+ ion images relative to heavier masses. A 3 minute, 20 µm square raster pre-sputter was applied to reduce H^+ background. Analysis was then carried out using a 15-20 µm spot. Secondary ions were analysed with a 25 µm image field. Analysis of quartz crystals at regular intervals during analysis was used to determine H^+ backgrounds (< 0.02 wt%).

The SIMS data was collected over 8 cycles with total count times of 30 s for ^1H and 80 s for ^{19}F, 40s for ^{35}Cl, and 16s for ^{30}Si, which was used for internal standardisation. ^1H counts were only recorded for the final 6 cycles to avoid any contamination. H_2O concentrations for the GSC glasses were calculated using a H_2O versus $^1H/^{30}Si$ calibration slope determined using analyses of BCR-2g (anhydrous) and standards St-1, St-2, and St-6 from Shishkina et al. (2010). Calibration slopes for F and Cl (F versus $^{19}F/^{30}Si$ x SiO_2 and Cl versus $^{35}Cl/^{30}Si$ x SiO_2) were determined using the composition of BCR-2g from by Marks et al. (2017). The analytical precision for H_2O (3.5%), F (8%) and Cl (16%) was constrained using five repeat measurements of GSC basalt TR164 11D-1g.

4 RESULTS

Our new SIMS and EPMA data represent the first systematic analyses of H_2O, F, S and Cl for well-characterised D-, N- and E-MORB erupted on the eastern GSC (geochemical divisions are the same as

those used in Gleeson et al. 2020), and thus expands the published volatile dataset to cover the entire section of the Galápagos plume-influenced ridge (Cushman et al., 2004; Ingle et al., 2010; Le Voyer et al., 2018; Michael, 1995).

4.1 DEGASSING, CONTAMINATION AND FRACTIONAL CRYSTALLISATION

The volatile contents of oceanic basalts are highly susceptible to modification by degassing, contamination and crystal fractionation (Dixon, 1997; Kendrick et al., 2015; Workman et al., 2006). All of the GSC samples analysed in this study were collected at water depths >1500 m and erupted under high enough pressure to minimise loss of H_2O to a vapour phase (Dixon, 1997; Iacovino et al., 2020; Shishkina et al., 2014). As a result, we estimate that degassing had only a minor influence on the H_2O content of these GSC basalts (generally <2% loss; see Supplementary Information).

An indication of the extent of magmatic interaction with seawater or hydrothermal brines, which can substantially influence the H_2O contents measured in submarine basalts (Kendrick et al., 2015), is provided by the Cl and K_2O concentrations of basaltic lavas. In the GSC basalts, Cl exhibits a large range (9 ppm to 3360 ppm) and almost all samples have Cl/K ratios that are much greater than those previously proposed for primary OIBs or MORBs (Fig. 2a; 0.01-0.08, with some regions up to 0.15; Kendrick et al., 2015; Le Roux et al., 2006; Michael and Cornell, 1998). We therefore suspect that GSC basalts have assimilated a Cl-rich component (that is, a brine).

We used the H_2O/Cl, K/Cl and F/Cl ratios of the GSC basalts, together with an assumed Cl/K ratio of 0.08, to evaluate and correct for the effects of brine assimilation on their H_2O contents (see Supplementary Information). Owing to the influence of brine assimilation on the Cl content of the GSC basalts, we do not attempt to constrain variations in the Cl/K or Cl/Nb ratio of their mantle source regions. Likewise, although S is commonly hypothesised to behave similarly to Dy during mantle melting (Fig. 2b; Peterson et al., 2017), recent studies have shown that concentrations of chalcophile elements (such as Se, Ag, and Cu) are required to truly evaluate the behaviour of S during mantle melting and fractional crystallisation (Reekie et al., 2019; Sun et al., 2020; Wieser et

al., 2020). Since chalcophile element data is not available for our samples, we focus on constraining only the H_2O and F systematics of the GSC mantle source regions.

To account for sub-ridge magma chamber processes, we have corrected the volatile data from the GSC basalts for fractional crystallisation (to 8 wt. % MgO), using the method outlined for major and trace elements by Gleeson et al. (2020) and mineral-melt volatile element partition coefficients published by Hauri et al. (2006) and Johnson (2006).

4.2 Variations in H_2O and F contents of GSC basalts

Our new SIMS data reveal that basalts from the GSC exhibit large variations in H_2O, with basalts from the western GSC reaching higher concentrations (0.10 to 1.08 wt.%; Cushman et al., 2004) than those on the eastern GSC (0.12 to 0.87 wt.%); this is a significant difference given the relatively small analytical uncertainty of the H_2O analyses (~3.5 %). Fluorine contents also show large variations in the GSC basalts; as with H_2O, F concentrations display a larger range in basalts from the western GSC (70 – 838 ppm; Ingle et al., 2010) compared to the eastern GSC (92 – 579 ppm). The highest concentrations of both H_2O (>0.4 wt.%) and F (>300 ppm) typically occur in basalts erupted between 89 and 92 ^{o}W (i.e. on either side of the Galápagos Transform Fault, Fig. 1), except for a single sample (ST7 17D-1g) collected from 86.13^{o}W on the eastern GSC (bathymetry data shows no evidence for a seamount or other topographic anomalies in this region; Ryan et al., 2009). Our new data collected from the western GSC displays comparable H_2O and F contents to similarly enriched samples previously analysed by Ingle et al. (2010) and Cushman et al. (2004), and confirms that our analyses are consistent with those from these previous studies.

Both H_2O and F exhibit strong positive correlations with indices of trace element enrichment (such as $[La/Sm]_n$) in the GSC basalts (Fig. 3; Supplementary Information). Importantly, the GSC basalts with the highest H_2O and F contents (ST7 17D-1g and TR164 26D-3g) also have anomalously high $\delta^{56}Fe$ values (Gleeson et al., 2020; Fig. 3). While Sr, Nd or Pb isotope data are not available for ST7 17D-1g,

we note that the volatile-rich sample TR164 26D-3g (90.95 °W) has enriched $^{87}Sr/^{86}Sr$, $^{143}Nd/^{144}Nd$ and Pb isotopic ratios relative to other GSC basalts.

5 CONSTRAINING THE VOLATILE CONTENT OF THE GSC MANTLE SOURCE

A commonly used method for determining the volatile concentrations in the mantle source region of oceanic basalts is to measure ratios of volatile and non-volatile trace elements that exhibit similar incompatibilities during melting and crystal fractionation (Cabral et al., 2014; Jackson et al., 2015; Koleszar et al., 2009; Michael, 1999; Saal et al., 2002). Widely used ratios include H_2O/La, H_2O/Ce, F/Nd, Cl/K and S/Dy (Cabral et al., 2014; Jackson et al., 2015; Koleszar et al., 2009; Peterson et al., 2017; Saal et al., 2002) although others have been suggested (e.g. F/Zr; Le Voyer et al., 2015). In this study we use the ratios H_2O/La and F/Nd to describe the volatile systematics of the different potential mantle components beneath the GSC (i.e. peridotite and pyroxenite). Using recent constraints from experiments at mantle conditions on the mineral-melt partitioning of H_2O and F (Dalou et al., 2012; Rosenthal et al., 2015), our mantle melting models indicate that H_2O displays similar compatibilities to La during melting of both source components (see Supplementary Information; H_2O partitioning data taken from Rosenthal et al. 2015). Fluorine is slightly less compatible than Nd during melting of a pyroxenitic source lithology and slightly more compatible during melting of a peridotitic source component (Supplementary Information; F partitioning data taken from Dalou et al. 2012). These results are consistent with observations from global MORBs and OIBs (e.g., Danyushevsky et al., 2000; Kendrick et al., 2017).

The H_2O/La ratios of the GSC basalts exhibit a negative correlation with indices of geochemical enrichment (such as $[La/Sm]_n$; Fig. 2c). Variations in the $[La/Sm]_n$ ratio of the GSC basalts could, theoretically, result from changes in the melt fraction of the mantle source; however, our mantle melting models indicate that the negative correlation between H_2O/La and $[La/Sm]_n$ is inconsistent with that predicted for melting of a single mantle source, as H_2O is slightly less compatible than La

306 during large amounts of mantle melting (Fig. S.9; Rosenthal et al., 2015). In addition, as the $[La/Sm]_n$
307 ratios of the GSC basalts have previously been shown to correlate with radiogenic and stable isotope
308 ratios (Schilling et al. 2003; Gleeson et al. 2020), we suggest that the H_2O/La ratio of the GSC basalts
309 may also be controlled by mixing of melts from multiple, lithologically-distinct mantle components.
310 Using the maximum and minimum H_2O/La ratios measured in plume-influenced basalts from the
311 GSC (excluding outliers), we estimate that the peridotitic and enriched (pyroxenitic) components in
312 the mantle source region of the GSC basalts have H_2O/La ratios of ~750 and ~350-400, respectively
313 (Fig. 2). These estimates are supported by the results of our mantle melting models (see
314 Supplementary File) utilising recent experimentally-determined mineral-melt partitioning data for
315 H_2O (Fig. 2; Rosenthal et al. 2015).

316 Unlike H_2O/La, the F/Nd ratio of the GSC basalts does not display a clear relationship with indices of
317 geochemical enrichment (e.g. $[La/Sm]_n$; Fig 2d). The eastern GSC basalts have an average F/Nd ratio
318 of 17.6 (±7.2; including literature data), which is slightly lower than the F/Nd ratio of the western
319 GSC basalts (20.0 ±7.3; Ingle et al., 2010). Notably, there is a large variation observed in the F/Nd
320 ratios of D- and N-MORBs from the western GSC (potentially due to the poor counting statistics of
321 EPMA analyses at low F concentrations; Ingle et al., 2010), with many of these basalts extending to
322 substantially higher F/Nd ratios than that observed in submarine basaltic glasses and naturally
323 quenched melt inclusions from the Galápagos Archipelago (Fig. 2d; Koleszar et al., 2009; Peterson et
324 al., 2017). Our new analyses for the eastern GSC basalts, however, reveal very similar F/Nd ratios to
325 those analysed from the Galápagos Platform (Fig. 2d; Peterson et al., 2017).

326 To convert the H_2O/La and F/Nd ratios of the GSC basalts into mantle source volatile concentrations
327 knowledge of the trace element compositions of the different mantle components that contribute to
328 the GSC basalts are required. In the modelling shown in Section 6, it is clear that the depleted
329 composition (i.e. low $[La/Sm]_n$ ratios) of the plume-influenced D-MORBs from the eastern GSC can be
330 reproduced by melting of a peridotitic component with the trace element composition of the

depleted DMM (Depleted MORB Mantle; Workman and Hart, 2005). Therefore, if we assume that the La concentration of the depleted peridotite component beneath the eastern GSC is ~0.134 ppm (Workman and Hart, 2005), and that this component is characterised by a H_2O/La ratio of ~750 (characteristic of the most-depleted plume-influenced GSC basalts), its H_2O concentration can be calculated to be ~100 ppm. Very similar estimates for the H_2O content of this component are obtained if H_2O/Ce is used in place of H_2O/La (~105 ppm H_2O; see Supplementary Information). Our estimate for the H_2O content of the depleted peridotitic component beneath the GSC is slightly lower than the H_2O content estimated by Gibson and Richards (2018; 150 ppm) and similar to the estimates of Michael (1988); Saal et al. (2002); Salters and Stracke (2004); and Shimizu et al. (2016,2019) for the depleted MORB source mantle.

The Pb-isotope compositions of basalts from the western GSC imply that they contain a small melt contribution from the enriched Wolf-Darwin Galápagos mantle plume component (Gibson et al., 2015; Ingle et al., 2010). The H_2O content of the peridotitic mantle source beneath the western GSC, however, remains uncertain owing to the lack of constraints on the trace element composition of the Wolf-Darwin component. Nevertheless, in the modelling shown below, we find that the trace element composition of N-MORBs located near the margin of plume influence along the western GSC, which are more enriched than basalts found at similar plume-ridge distances on the eastern GSC, can be produced by melting of moderately enriched mantle peridotite. We calculated this as a 90:10 mixture of the depleted DMM (Workman and Hart, 2005) and the enriched mantle component proposed by of Donnelly et al. (2004). Using this source composition, with a La content of 0.194, we estimate the H_2O content of the peridotitic mantle source beneath the western GSC is ~145 ppm (H_2O/La ~750). Importantly, models of mantle melting involving this hypothesised peridotitic component can reproduce both the trace element and H_2O contents of the western GSC N-MORBs located near 95.5°W (Fig. 2; Fig. 4).

Large uncertainties in the composition of recycled oceanic crust, and the relative contribution of ambient mantle peridotite and melts of a recycled crustal component to the formation of secondary pyroxenites, mean that the trace element and H_2O content of a pyroxenitic component are difficult to constrain. In our mantle melting models, we tested various potential solutions for the trace element composition of the pyroxenitic source that might contribute to the GSC basalts, and determined that a trace element composition similar to that proposed for the KG1 pyroxenite by Lambart (2017) can recreate the trace element systematics and crustal thickness estimates of the GSC (Ce, and Nd contents decreased by ~10% from the Lambart, 2017 estimate). Our estimated pyroxenitic source composition has a La content of ~1.415 ppm that, alongside an estimated H_2O/La ratio of ~350-400 for this source component, provides a H_2O estimate of 495 – 565 ppm. Our new data confirms that in the Galápagos mantle plume the enriched (pyroxenitic) component has a higher H_2O content than the isotopically-depleted component (~100 ppm).

Our new estimates for the H_2O contents of the GSC peridotitic components are uninfluenced by the choice of ratio to describe the behaviour of H_2O (i.e., H_2O/La or H_2O/Ce). However, the H_2O estimates derived from the enriched (pyroxenite) component are higher if we use the ratio H_2O/Ce (3.81 ppm Ce, H_2O/Ce ~ 170 and, therefore, H_2O ~650 ppm) rather than H_2O/La (H_2O ~495 – 565 ppm). However, we note that both the H_2O/La and H_2O/Ce contents of the GSC can be recreated by our mantle melting models when the pyroxenitic source component has a H_2O content around ~550 ppm (Fig. 2c; Supplementary Information).

If we assume that F acts comparably to Nd during mantle melting (which is consistent with some experimental data and the strong correlation between these elements in many MORB suites; Dalou et al. 2012; Kendrick et al. 2017), then the F content of the depleted mantle component beneath the eastern GSC can be estimated from its Nd content (assumed to be ~0.48 ppm, equivalent to that of the depleted DMM; Workman and Hart, 2005) and the F/Nd of the depleted eastern GSC basalts (~16 – 18). The results of these calculations give a F content of 7.7 – 8.7 ppm, the upper limit of

which is shown to recreate the F/Nd systematics of the eastern GSC basalts in our models of melting a 2-component mantle (Fig. 2d).

Similarly, taking a source Nd concentration of ~0.56 ppm (calculated assuming a 90:10 mixture of depleted DMM and enriched mantle for the western GSC peridotite), we can constrain the F content of the peridotitic component beneath the western GSC to 8.4 – 15.6 ppm (assuming a characteristic F/Nd ratio of 15-30), consistent with the western GSC data (Ingle et al., 2010). Finally, if we take the F/Nd ratio of the most enriched GSC basalts (20 – 21.5) to be characteristic of the pyroxenitic mantle source component, the source F concentration is calculated to be 80 – 86 ppm (source Nd concentration of 4.00 ppm). However, our new mantle melting models that incorporate experimental constraints on F partitioning during mantle melting (Dalou et al., 2012) reveal that a pyroxenitic source F concentration >80 ppm overestimates the F/Nd ratio of the most enriched GSC basalts (owing to the slightly more incompatible nature of F than Nd during melting of a pyroxenitic lithology; Fig. 2d; Supplementary Information). To provide more robust constraints on the F content of the pyroxenitic mantle source, we have iteratively adjusted the concentration of F in our mantle melting models until the model predictions (generated by varying the proportion of plume-derived channelised melt to the GSC; see Section 6) matched the GSC data. The results indicate that our new data is best matched when the pyroxenitic F content is set at ~70 ppm.

6 NUMERICAL MODELS OF GALÁPAGOS PLUME-RIDGE INTERACTION

6.1 SIMULATING MANTLE MELTING

Early models of plume-ridge interaction related compositional variations in plume-influenced MORBs to chemical heterogeneity on the scale of 10s to 100s of km in the sub-ridge mantle (i.e. erupted magma compositions are directly related to the bulk composition of the underlying mantle; Schilling, 1991; Schilling et al., 2003, 1982; Verma and Schilling, 1982). Such models suggested that

isotopically and incompatible trace element enriched plume material flows towards, and then along, the ridge axis where it becomes progressively diluted by mixing with ambient asthenosphere.

These early models recreated some of the geochemical features that are observed along plume-influenced ridges; however, dynamical models of plume-ridge interaction predict no significant solid-state mixing between plume and ambient mantle (Farnetani and Richards, 1995; Ito et al., 2003, 1997). For this reason, more recent studies of plume-ridge interaction have focused on a second class of model, where mantle heterogeneity is important on length-scales of ~1 km or less (Ingle et al., 2010; Ito and Mahoney, 2005). In this type of model, the solid sub-ridge mantle is composed of a near constant mixture of enriched, hydrous peridotite or pyroxenite 'blebs' in a depleted (anhydrous) peridotite matrix. Owing to their different volatile contents and/or lithological properties, the enriched blebs undergo melting at greater depths than the surrounding anhydrous peridotite (Ingle et al., 2010; Ito and Mahoney, 2005). Previous studies that have applied these models to the GSC have concluded that variations in basalt chemistry and crustal thickness are due to intermediate scale variations in mantle flow and/or melt extraction from the underlying mantle (Ingle et al., 2010; Ito and Bianco, 2014; Ito and Mahoney, 2005; Shorttle et al., 2010).

To test the plausibility of a mixed lithology mantle in Galápagos plume-ridge interaction, we use the pymelt module of Matthews et al. (2020), which simulates melting of peridotite and silica-undersaturated pyroxenite (KG1). We build on this model by calculating the trace element composition of basaltic melts formed beneath the ridge axis (see Supplementary Information) and including calculations that account for the contribution of channelized melts formed by melting of a pyroxene-rich mantle component in the Galápagos plume stem (Gleeson et al., 2020). By simulating the melting of a mixed lithology mantle our models differ from those of previous studies that have considered only volatile-bearing peridotite source components (Gibson and Richards, 2018; Ingle et al., 2010).

Our new models allow us to test the influence of the rate of mantle upwelling; depth at which melting ceases; and the contribution of channelised, plume-derived melts on the crustal thickness of the ridge and the trace element chemistry of the GSC basalts (see Supplementary Information for full model details). The initial non-volatile trace element composition of the various mantle components beneath the GSC are set as the depleted DMM (Workman and Hart, 2005), a 90:10 mixture between the depleted DMM and an enriched mantle component (Donnelly et al., 2004), and a similar composition to that estimated for the KG1 pyroxenite by Lambart (2017) for the eastern GSC peridotite component, the western GSC peridotite component, and the enriched pyroxenitic component, respectively. In all of our models, the trace element partition coefficients were taken from Gibson and Geist (2010) and mineral-melt partition coefficients for H_2O and F were taken from recent experimental data (Dalou et al., 2012; Rosenthal et al., 2015).

We recognise that the parameterisations of silica-undersaturated melting in pymelt do not consider the effects of volatiles on the pyroxenite solidus. Analyses of natural samples of mantle pyroxenites have, however, shown that they have a greater capacity to host volatiles than peridotites (Gibson et al., 2020). The influence of elevated H_2O contents on the pyroxenitic solidus remains uncertain, although some experimental data indicates that the depression in the solidus temperature caused by the presence of H_2O in a pyroxenitic mantle source is less than that seen in peridotitic source components (Sorbadere et al., 2013). Nevertheless, more experimental work is required to accurately parameterise the effects of H_2O on pyroxenite melting, as has been done for peridotites (Katz et al., 2003). In our forward models of fractional melting we have used a H_2O estimate of 550 ppm for the pyroxenite source, as this reproduces the volatile vs trace element systematics of the GSC basalts (see Section 5). We accept, however, that because of uncertainties in the depth of melting of volatile-bearing pyroxenite this is a non-unique solution.

Using our new models of mantle melting, we calculate the hypothetical composition of magmas produced at ~0.05° intervals along the GSC, with variations in key mantle parameters (such as T_P; U_r

– the maximum horizontal velocity of mantle material exiting the melting zone (Ingle et al., 2010; Ito and Mahoney, 2005); and the contribution of channelised plume-derived melts) tested to determine the dominant mechanism of plume-ridge interaction in the Galapagos. First, we examine the extent to which the long and short length-scale geochemical and geophysical features of plume-ridge interaction on the GSC can be recreated if we assume only solid-state flow between the Galápagos mantle plume and GSC, as proposed by Ingle et al. (2010), Shorttle et al. (2010) and Ito and Bianco (2014). We then highlight areas where solid-state plume-ridge interaction models poorly match the available data, and examine whether additional transport of volatile-rich melts in long-lived melt channels (Gibson and Richards, 2018) can account for these discrepancies.

6.2 Along-ridge variations in GSC basalt geochemistry and crustal thickness predicted by solid-state flow

In the models of solid-state plume-ridge interaction shown below, it is assumed that variations in basalt chemistry and crustal thickness along the GSC are related to changes in the rate of mantle flow below the anhydrous peridotite solidus and/or variations in source ratios (Cushman et al., 2004; Gibson and Richards, 2018; Ingle et al., 2010; Ito and Bianco, 2014; Maclennan et al., 2001; Shorttle et al., 2010). Variations in mantle upwelling velocity are hypothesized to occur as a result of the excess buoyancy flux of mantle plumes and the rapid increase in mantle viscosity associated with olivine dehydration following the onset of mantle melting (Hirth and Kohlstedt, 2003, 1996). In addition, although dynamical models of plume-ridge interaction indicate that that there will be limited mixing between plume material and the surrounding ambient mantle in the asthenosphere (Ito et al., 1997), variations in source proportions beneath the GSC are considered owing to the clear spatial heterogeneity in the composition of the Galapagos mantle plume (Gleeson et al. 2021; Harpp and Weis, 2020; Harpp and White, 2001; White et al., 1993).

In the following solid-state plume-ridge interaction models, the relative rate at which mantle material exists the melting region at the base of the melt column ($U_{r\text{-}max}$; horizontal velocity relative to a scenario where no active upwelling is present) is assumed to follow an exponential decay curve

with longitude (Table 1), with maximum values close to the GTF. This relationship (between $U_{r\text{-}max}$ and longitude) is selected following the study of Ingle et al. (2010) and qualitatively follows the change in mantle flow velocities predicted by the numerical models of Bianco et al., (2013) and Ito and Bianco (2014). Similarly, we test various relationships between longitude and the mantle potential temperature (T_p), the mass fraction of pyroxenitic material in the source and the pressure at the base of the lithosphere/top of the melt column.

We iteratively adjusted these parameters until our models produced a satisfactory match to both the composition of the GSC basalts and the crustal thickness estimates of Canales et al. (2002) and Mittelstaedt et al. (2014). Example model results are shown in Figure 4 and indicate that solid-state plume-ridge interaction produces an excellent match to the composition of most basalts erupted west of 86°W on the eastern GSC, and the D-MORBs and N-MORBs located on the western GSC. In addition, the model results reveal clear differences between the eastern and western GSC. For example, to generate the greater crustal thickness of the oceanic crust produced along the eastern GSC (Mittelstaedt et al., 2014), our models indicate that the mantle potential temperature beneath the eastern GSC is ~5 °C higher than beneath the western GSC, and that there are slight differences in the mantle flow velocities driven by buoyant upwelling of the plume material. Additionally, our results indicate that the pressure at the top of the melting region is greater in regions adjacent to the GTF, possibly owing to conductive cooling effects of the cold lithospheric material of the transform fault (Le Voyer et al., 2015) and the increased proportion of pyroxenite in the mantle source (Brunelli et al., 2018). This increase in the pressure of melt termination is required to avoid a 'run-away' increase in the crustal thickness of the ridge in regions where the largest excess mantle flow velocities are predicted..

Figure 4 also highlights several pitfalls that are associated with solid-state plume-ridge interaction models that account for lateral variations in mantle flow. For example, modelled crustal thickness increases systematically along the western GSC towards the GTF, which is qualitatively consistent

503 with the crustal thickness variations predicted in numerical simulations of mantle flow for on-axis (or
504 near-axis) mantle plumes (e.g. Iceland; Bianco et al., 2013). Recent studies have, however, shown
505 that there are three ~20 km wide regions between ~92.5°W and the GTF with crustal thickness
506 anomalies of ~1 km (Mittelstaedt et al., 2014), which our simple model of solid-state plume-ridge
507 interaction cannot capture (Fig. 4). In addition, although the solid-state plume-ridge interaction
508 model shown in Fig. 4 accurately recreates the chemistry of the western GSC N-MORBs located west
509 of 92.5 °W and east of 91.8 °W, they are not able to recreate the composition of the more enriched
510 basalts located between 92.5°W to 91.8°W, or the compositions of anomalously enriched basalts
511 that are present between 89.5 and 92°W on the GSC.

512 Some of these discrepancies may be addressed if we consider non-symmetric spreading of solid
513 plume material. One possible mechanism that might facilitate such flow is thermal erosion of a sub-
514 lithospheric channel between the mantle plume and adjacent ridge (Kingsley and Schilling, 1998;
515 Schilling, 1991). However, geophysical and petrological estimates indicate that there are no areas of
516 significant (i.e. >10 km) lithospheric thinning beneath the volcanic lineaments connecting the
517 western GSC to the Galapagos Archipelago (Gibson and Geist, 2010; Harpp et al., 2014c). Therefore,
518 any thermal erosion of the lithosphere beneath the northern Galapagos is unlikely to be sufficient to
519 trap plume material and influence plume outflow (cf. Gibson et al., 2015). In addition, some of the
520 offsets between our model predictions and the GSC data may result from the use of a 2D model
521 scenario to describe a 3D system. In particular, the influence of transform faults on upper mantle
522 dynamics is not considered here, but could influence the composition of basalts erupted close to
523 these structures (Weatherley and Katz, 2010). Nevertheless, we believe that this is unlikely to
524 account for the shortcomings of the solid-state plume ridge interaction models.

525 6.3 CHANNELISED FLOW OF H_2O-RICH MELTS TO THE GSC

526 Numerical models of mantle melting beneath oceanic spreading centres have shown that highly
527 permeable melt channels are a natural consequence of melting during upwelling of a heterogeneous

mantle (Katz and Weatherley, 2012; Weatherley and Katz, 2012). As channelised melt flow is expected to restrict chemical interaction of channelised melts with the surrounding mantle (Weatherley and Katz, 2012) it might represent an efficient method of transporting geochemically enriched material to nearby spreading centres. In addition, highly-permeable melt channels have been shown to be thermodynamically stable over distances up to ~1500 km (for channels ~50 – 60m in radius) and the transport timescales of volatile-rich melts in these channels are significantly lower than the timescales required by U-series disequilibria (Kokfelt et al., 2005; Mittal and Richards, 2017). Therefore, conceptual models involving the delivery of plume-derived compositionally-enriched melts to MORs in highly permeable melt channels have been proposed for the Galápagos and other sites of plume-ridge interaction worldwide (Gibson et al., 2015; Gibson and Richards, 2018; Mittal and Richards, 2017). In these models, the primary factor driving the migration of melts from the stem of the upwelling plume (>60 – 80 km depth) to the sub-ridge mantle (<40-60 km depth) is melt buoyancy. Melt channelisation was likely initiated when the Galápagos plume was on-axis (at >5 Ma) and has been maintained during ridge migration away from the plume stem (Gibson et al. 2015).

6.3.1 Variations in the supply of channelized melts to the western and eastern GSC

The solid-state plume-ridge interaction models described in Section 6.2 require relative mantle flow velocities ($U_{r\text{-}max}$) of ~6-8 to explain the geochemical and geophysical signatures of plume-ridge interaction between 90.5°W and 90.8°W (Fig. 4). Values of $U_{r\text{-}max}$ up to ~15 have previously been suggested, based on the buoyancy flux of the Galápagos mantle plume (Ingle et al., 2010; Sleep, 1990). However. recent numerical simulations of Galápagos plume-ridge interaction indicate that along ridge variation in the maximum relative upwelling velocity is relatively limited (a factor of 3; ~75 mm/yr compared to a velocity of ~25 mm/yr for passive mantle upwelling; Ito and Bianco, 2014), a result consistent with the velocities calculated for buoyancy driven upwelling by Gibson and Richards (2018; 40 mm/yr).

In the following models we assume that: (i) the change in the relative mantle flow velocity below the anhydrous peridotite solidus is small ($U_{r\text{-}max}$ <1.5 – 2.5); and (ii) variations in the geochemical and geophysical signatures of plume-ridge interaction along the GSC are primarily derived from slight changes in T_P and/or the supply of channelised melts from the Galápagos plume stem (Table 1). The volatile and non-volatile trace element composition of the channelised melts are calculated as the non-modal aggregated fractional melt of the enriched (pyroxenitic) mantle component (see Supplementary Information for detailed methods). We assume that the melt channels form at depths below the anhydrous peridotite solidus (>2.5 - 3 GPa at T_P = 1400^{o}C) and various different values for the pressure of channel initiation/formation were tested.

The crustal thickness and geochemical characteristics of the eastern GSC are generally well-matched by our solid-state models of plume-ridge interaction. Nevertheless, we recognise that this is not a unique solution as these observations can also be reproduced if we model an exponential decrease in the proportion of channelized melts supplied to the eastern GSC with increasing distance to the centre of plume upwelling (Fig. 5). In this model, the decrease in the supply of channelized, enriched melt to the eastern GSC with increasing distance to the Galapagos plume can be primarily assigned to the changing angle at which melt channels are likely to intersect the ridge axis (i.e. near the GTF melt channels may be orientated roughly perpendicular to the ridge axis but this orientation is not maintained further east; Fig. 6), resulting in a reduction in the influence of channelised melt transport to the each segment of the eastern GSC. This hypothesis shares many similarities to the model proposed for solid-state plume-ridge interaction by Shorttle et al. (2010), but has the advantage of being able to simultaneously explain the enriched geochemical signatures along the GSC and the depleted isotopic compositions of the island of Marchena and Genovesa in the Northern Galápagos Volcanic Province (Gibson et al., 2015; Harpp et al., 2014c).

At the closest point to the Galápagos Archipelago, the eastern GSC is located only ~100-150 km north of the centre of plume upwelling, identified at 100 km depth in the seismic tomography study

of Villagomez et al. (2014). In their theoretical study, Mittal and Richards (2017) showed that over such short plume-ridge separation distances, melt channels ~5 m in radius are likely to be thermodynamically stable (assuming a constant heat flux source). This channel radius is within the range observed in dunitic/melt channels observed in ophiolites worldwide (e.g., dunitic channels in the Oman ophiolite can reach 200 m across; Kelemen et al., 1997). We suggest, therefore, that the delivery of compositionally-enriched melts to the eastern GSC in a dense network of small melt channels embedded within a spreading puddle of plume material, as envisaged by Gibson et al. (2015), might lead to effective homogenization of mantle melts over the length-scale at which variability in geochemical compositions has currently been measured. A steadily declining supply of enriched melts is observed on the eastern GSC with increasing distance to the Galápagos mantle plume, owing to the change in the intersection angle of the melt channels and the ridge as well as the declining proportion of melt channels that will remain thermodynamically stable over the increased melt transport distances. The continued presence of channelised melts along the whole of the eastern GSC, even if only in very small proportions (<1%), maintains the possibility that anomalously enriched basalts can be observed at the surface at plume-ridge interaction distances in excess of 300 – 400 km (see Section 6.3.2). However, while the geochemical and geophysical features observed on the eastern GSC can be produced by both solid-state and melt transport models of plume ridge interaction, many of the discrepancies between the GSC data and solid-state models of plume-ridge interaction occur on the western GSC (e.g. the composition of basalts located between the 92.5°W and 91.8 °W).

Our modelling reveals that the geochemical and geophysical signatures of plume-ridge interaction on the western GSC cannot be produced by a similar model to that used to recreate the eastern GSC data (i.e. a gradually decreasing supply of channelised melts with increasing plume-ridge distance). Instead, we find that the discrepancies between the western GSC geochemical and geophysical data and our solid-state plume-ridge interaction models can be overcome by modelling a low level of channelised melt contribution to the western GSC between ~93°W and the GTF (<10%) and focused

delivery of additional channelized melts to the western GSC beneath each of the three volcanic lineaments in the northern Galápagos (Fig. 5), as proposed by Mittal and Richards (2017) and Gibson and Richards (2018). In the model used here, the proportion of channelized melt supplied to the western GSC beneath each of the lineaments is assumed to follow 3 overlapping normal distributions, where the greatest rate of supply occurs at the intersection of each of the three volcanic lineaments with the GSC (92.25°W, 91.8°W, 91.3°W). The results provide an excellent match to the geochemical data (including volatiles) from the western GSC and reproduce the short length-scale variations in crustal thickness observed at the intersection of each volcanic lineament with the western GSC (Fig. 5; Mittelstaedt et al., 2014). It is important to note, however, that the compositional variability between the different seamounts and islands that make up the three volcanic lineaments indicates that their magmatic systems are locally complex (Harpp et al., 2014c).

Notably, the models used to recreate the geochemical and geophysical signatures of plume-ridge interaction along the western and eastern sections of the GSC are very different, although similar levels of geochemical enrichment are observed on both ridge segments. We propose that the differences may arise from the greater plume-ridge distance of the western GSC compared to the eastern GSC (~100 km greater). Specifically, we suggest that the large plume-ridge interaction distance of the western GSC results in the amalgamation of several smaller melt channels into three main channels that are located beneath each volcanic lineament (and thus localised delivery of channelised melt to the ridge axis). This coalescence may help to maintain the thermodynamic stability of the melt channels over the greater plume-ridge distance (Fig. 6; Mittal and Richards, 2017), and is consistent with the amalgamation of high porosity (channelised) regions observed in numerical models of mantle melting (e.g. Katz and Weatherley, 2012). Nevertheless, the coincidence of a ~10 km wide crustal thickness anomaly (Mittelstaedt et al., 2014) and two anomalously volatile-rich samples (TR164 6D-1g and 2g, which lie outside the compositions predicted by our along-ridge models; Fig. 5) on the eastern GSC at 89.59°W indicate that localised variations in the volume of melt delivered to the eastern GSC exist. In addition, the sample density along the eastern GSC is lower

630 than that along the western GSC, which raises the possibility that other short length-scale
631 geochemical heterogeneities in the region between 89.59°W and 90.8°W may be present, but are
632 unsampled. As such, more data is required to confirm that differences in the nature of melt
633 channelisation to the western and eastern GSC control the geochemical and geophysical features of
634 plume-ridge interaction in the Galápagos.

635 ### 6.3.2 Anomalously enriched GSC basalts

636 The above models of plume-ridge interaction via channelised transport of volatile-rich melts
637 accurately recreate the broad-scale, and some of the short length-scale, geochemical and
638 geophysical features of plume influence on the GSC. There are, however, a series of basalts located
639 along plume-influenced segments of the GSC (and in other regions of plume-ridge interaction
640 worldwide) that display compositions which are too enriched to be explained by any of the models
641 outlined above (e.g. TR164 6d-1g at 89.59 °W; Gibson and Richards, 2018). These anomalously
642 enriched basalts, which typically contain $[H_2O]_{(8)}$ contents >0.4 wt%, have previously been explained
643 through the localised delivery of large volumes of channelised melt to the ridge, overwhelming the
644 contribution of more depleted melts formed in the shallow mantle (Gibson and Richards, 2018;
645 Mittal and Richards, 2017). To build on this previous work, we compared the results of our mantle
646 melting models that incorporate the presence of channelised, plume-derived melts to the
647 composition of the anomalously enriched basalts located along the GSC.

648 In detail, we calculated the Root Mean Squared Error (RMSE) between our mantle melting models
649 and each of the anomalously enriched GSC basalts. The mantle potential temperature of the
650 Galapagos plume (where the channelised melts are being formed) is set at 1400 °C in all calculations,
651 and we tested the fit between our models of the composition of the GSC when the percent
652 contribution of channelised melt is varied between 0 and 50%, and the pressure of channel
653 formation is varied between 2.8 and 3.6 GPa. This pressure range was chosen as initial models
654 showing the influence of incorporating plume-derived channelised melts demonstrated that channel

formation at lower pressures is unable to recreate the high $[La/Sm]_n$ ratio of the anomalously enriched GSC basalts (Fig. 7a). The proportion of pyroxenite in the Galapagos plume stem was set at ~20% (Gleeson et al. 2021).

The model calculations demonstrate that the anomalously enriched basalts from the GSC, which have $[H_2O]_{(8)}$ contents >0.4 wt%, likely contain a >15% contribution of channelised, plume-derived melts (Fig. 7). However, the large proportion of channelised melt required to recreate the composition of these anomalously enriched basalts is inconsistent with the magnitude of the crustal thickness anomalies found in these locations (Mittelstaedt et al., 2014). For example, at ~89.59 ^{o}W on the eastern GSC, where a crustal thickness anomaly of ~1 km is observed (~9.5 km thick crust compared to the model predictions of ~8.5 – 9 km), the ~15% contribution of channelised melt required to reproduce the geochemical signature of the highly enriched GSC basalts would, in theory, generate a crustal thickness anomaly >1.5 km (Fig. 7). The discrepancy between the predicted and observed crustal thickness is even greater at the location of sample TR164 26D-3g (90.95 ^{o}W) where no crustal thickness anomaly is observed, but a >30% contribution of channelised melt is required to reproduce the trace and volatile element systematics of the erupted basalt.

We therefore suggest that the extremely high proportion of channelized melt required to generate the composition of the most volatile-rich GSC basalts may result from inefficient mixing of these channelised melts with those produced at shallower depths in the sub-ridge mantle (Fig. 8). A scenario that is consistent with the proposed chemical isolation of high-pressure channelised melts with the surrounding mantle peridotite during magma transport (Katz and Weatherley, 2012; Keller and Katz, 2016). In this scenario, volatile-rich basaltic magmas may reach the surface even in regions where there is a relatively low flux of channelized plume-derived melts to the GSC (Fig. 8). In fact, the low melt flux at large plume-ridge interaction distances (e.g. sample ST7 17D-1g; 86.13 ^{o}W), and locations that are proximal to large transform faults (e.g. samples TR164 26D-3g; 90.95 ^{o}W, respectively), might restrict the formation of a steady-state magma chambers (Le Voyer et al., 2015;

Sinton and Detrick, 1992). As a result, it is possible that magma homogenisation is subdued at these locations, increasing the probability of enriched basalts being observed at the surface (Langmuir and Bender, 1984; Le Voyer et al., 2015).

7 QUANTIFYING THE OUTFLUX OF H_2O ON PLUME-INFLUENCED SECTIONS OF THE GALÁPAGOS SPREADING CENTRE

Our new volatile data expand the small number of analyses previously published for the eastern GSC (e.g. Byers et al., 1983), and extend the existing GSC database of volatile element analyses to cover the entire region of plume-influenced ridge. Nevertheless, for many basalts erupted along plume-influenced sections of the GSC volatile data are absent and we thus use the available fractional crystallisation corrected H_2O data from both the eastern and western GSC to identify a non-volatile trace element proxy that can be used to estimate the H_2O contents of the remaining GSC basalts.

The $[H_2O]_{(8)}$ (that is, the water concentration of each sample once it has been fractional crystallisation corrected to 8 wt% MgO) and $[Sm/Yb]_n$ contents of basalts from both the western and eastern GSC display a very strong, positive correlation (r^2=0.907; Fig 3a). As such, we use the $[Sm/Yb]_n$ ratio of the GSC basalts as a proxy for their fractionation corrected H_2O contents ($[H_2O]_{(8)}$). $[Sm/Yb]_n$ is chosen rather than $[Ce/Yb]_n$, as suggested by Gibson and Richards (2018), because our new data shows a small number of highly-enriched basalts from the western GSC have slightly higher $[H_2O]_{(8)}$ at a given $[Ce/Yb]_n$ than the other GSC basalts (Fig. 3b). As a result, the correlation between $[H_2O]_{(8)}$ and $[Ce/Yb]_n$ is subtly different for basalts from the eastern and western GSC (gradients of 0.142 and 0.162, respectively; Fig. 3b).

Taking our new volatile data from the eastern GSC, together with published volatile data from the western GSC (Cushman et al., 2004; Ingle et al., 2010), and estimated volatile contents based on the trace element content of additional GSC basalts (Christie et al., 2005), we can use our 2 component

models of plume-ridge interaction to calculate the outflux of H_2O from plume-influenced sections of the GSC. This is achieved using our along-ridge mantle melting models that incorporate the influence of channelised melt transport and accurately recreate the trace element composition and crustal thickness of the plume-influenced GSC alongside the following equation:

$$H_2O^{flux}(kg/(m.yr)) = (C_{H2O}^{mix}(ppm) \times 10^{-6}) \times SR\ (m/yr) \times CT\ (m) \times 2900(kg/m^3)$$

Where C_{H2O}^{mix} is the H_2O concentration of the fully homogenized primary mantle melts and *CT* is the crustal thickness produced at each calculation interval along the GSC (calculation step size of ~0.05°). *SR* represents the spreading rate of the GSC (Schilling et al., 2003), and the density of the melt phase is assumed to be ~2900 kg/m^3.

Our results indicate that incorporation of enriched material from the Galápagos mantle plume causes the flux of H_2O to increase by a factor of 3 from 86°W to 90.8°W on the eastern GSC (Fig. 9). On the western GSC, the flux of H_2O is greatest in regions where the volcanic lineaments intersect the GSC, and the maximum flux of H_2O from any part of the western GSC is similar to the maximum H_2O flux along the eastern GSC (~4000 kg.m^{-1}.yr^{-1}; Fig. 9). In addition, our calculations show that volatile-rich channelized melts contribute up to ~60% of the H_2O and F outflux, from localised regions of the plume-influenced GSC (Fig. 9; Fig. S.8). Overall, melt channelisation may account for ~35% of the H_2O outflux from the western GSC between 90.8°W and 92.5°W and ~25% of the H_2O outflux between 86°W and 90.8°W on the eastern GSC.

While transport of volatile-rich melts to the GSC has a clear influence on the H_2O and F concentrations of the erupted magmas, little to no variations are seen in the $^3He/^4He$ ratio of these basalts (Graham et al., 2014). This observation requires that melts reaching the GSC have much lower $^3He/^4He$ than those forming deep in the plume beneath the western Galápagos Archipelago. The lack of a primordial $^3He/^4He$ signature in plume-influenced GSC basalts may be because: (i) rapid vertical transport of high-pressure melts with elevated $^3He/^4He$ ratios is restricted to the vicinity of the plume stem (Kurz and Geist, 1999; Villagómez et al. 2014; Peterson et al. 2017); or (ii) the 'deep'

plume-stem melts that are being transported laterally to the ridge via channelised flow may be derived from blebs of recycled lithosphere (Gleeson et al., 2020) with similar or lower $^{3}He/^{4}He$ ratios to MORBs (e.g. Day et al., 2015).

8 CONCLUSIONS

Our study uses new analyses of volatiles (H_2O, F, Cl, and S) in basaltic glass chips from the Galápagos Spreading Centre, as well as two-component mantle melting models, to investigate the nature and dynamics of plume-ridge interaction in the Galápagos. The results of this study can be summarized in 4 key points:

1. Solid-state transfer of plume material between the Galápagos mantle plume and adjacent GSC can account for some of the long length-scale (~100 – 1000 km wide) geochemical and geophysical signatures of plume-ridge interaction. However, solid-state plume-ridge interaction models cannot easily explain the presence of short length-scale (<10 km) geochemical and geophysical heterogeneities.

2. The long and short length-scale features of plume-ridge interaction in the Galápagos are readily explained by plume-ridge interaction models that include the transport of volatile-rich melts to the GSC in melt-dominated channels. We hypothesise that the nature of melt transport is very different between the eastern and western GSC. This difference, where a large number of small melt channels connect the eastern GSC to the Galápagos mantle plume, but the western GSC is connected via a smaller number of much larger melt channels, might be related to the increased plume-ridge distance of the western GSC compared to the eastern GSC.

3. One key feature of plume-influenced ridge segments is the presence of anomalously enriched basalts, i.e. those that are substantially more enriched with respect to their trace

element contents than their neighbouring basalts (Gibson and Richards, 2018). The highly enriched basalts on the GSC also have anomalously-high Fe isotope ratios that have been interpreted as reflecting large contributions of melt from a pyroxenitic mantle component within the Galápagos plume (Gleeson et al., 2020). While we acknowledge that the role of pyroxenite is controversial, and more work needs to be done, the key findings of our models for the mechanisms of plume-ridge interaction are, to a large extent, independent of the source lithology chosen for the enriched mantle component in the source region of the GSC basalts (i.e. peridotite vs pyroxenite).

4. Our new mantle melting models indicate that the composition of the GSC basalts are controlled by the incomplete mixing of channelised, volatile-rich melts from the Galápagos mantle plume with more depleted melts formed in the sub-ridge mantle. They also suggest that the most enriched basalts from the GSC may contain a >40% contribution from channelized, plume-derived melt.

5. Our results indicate that plume-ridge interaction causes the H_2O flux out of the GSC to vary by a factor of ~3, with the greatest outflux observed on the eastern GSC near the Galápagos Transform Fault or at the intersections of volcanic lineaments with the western GSC (up to ~4000 $kg.m^{-1}.yr^{-1}$). We suggest that delivery of volatile-rich channelised melts to the ridge axis might account for up to ~60% of the H_2O flux out of these regions.

ACKNOWLEDGEMENTS

M.L.M.G. was supported by a NERC (Natural Environmental Research Council) Research Training Student Grant (NE/L002507/1) and a Research Fellowship funded by the Royal Commission for the Exhibition of 1851. S.A.G. was supported by grant RG57434 for research in Galápagos. We are grateful to Iris Buisman and Richard Hinton for assistance with EPMA and SIMS analysis, respectively. The Secondary Ion Mass Spectrometry analysis was carried out at the Edinburgh Ion Microprobe

Facility (award IMF622/0517). We thank Mike Stock for his help with SIMS data collection and early discussions about the project. We are also grateful to Mark Richards and Tushar Mittal for sharing their thoughts on plume-ridge interaction, together with Karen Harpp, Peter Michael and an anonymous reviewer whose constructive comments greatly improved the quality of our manuscript.

DATA AND CODE AVAILABILITY

Data collected in this study, and the code used to analyse the data, can be found through https://zenodo.org/badge/latestdoi/379869011

REFERENCES

Adam, J., Turner, M., Hauri, E.H., Turner, S., 2016. Crystal/melt partitioning of water and other volatiles during the near-solidus melting of mantle peridotite: Comparisons with non-volatile incompatible elements and implications for the generation of intraplate magmatism. Am. Mineral. 101, 876–888. https://doi.org/10.2138/am-2016-5437

Asimow, P.D., Langmuir, C.H., 2003. The importance of water to oceanic mantle melting regimes. Nature 421, 815–820. https://doi.org/10.1038/nature01429

Behn, M.D., Sinton, J.M., Detrick, R.S., 2004. Effect of the Galápagos hotspot on seafloor volcanism along the Galápagos Spreading Center (90.9–97.6°W). Earth Planet. Sci. Lett. 217, 331–347. https://doi.org/10.1016/S0012-821X(03)00611-3

Bianco, T.A., Ito, G., van Hunen, J., Mahoney, J.J., Ballmer, M.D., 2013. Geochemical variations at ridge-centered hotspots caused by variable melting of a veined mantle plume. Earth Planet. Sci. Lett. 371–372, 191–202. https://doi.org/10.1016/j.epsl.2013.03.050

Blacic, T.M., Ito, G., Canales, J.P., Detrick, R.S., Sinton, J., 2004. Constructing the crust along the Galapagos Spreading Center 91.3°-95.5°W: Correlation of seismic layer 2A with axial magma lens and topographic characteristics. J. Geophys. Res. Solid Earth 109. https://doi.org/10.1029/2004JB003066

Braun, M.G., Sohn, R.A., 2003. Melt migration in plume–ridge systems. Earth Planet. Sci. Lett. 213, 417–430. https://doi.org/10.1016/S0012-821X(03)00279-6

Brunelli, D., Cipriani, A., Bonatti, E., 2018. Thermal effects of pyroxenites on mantle melting below mid-ocean ridges. Nat. Geosci. 11, 7.

Byers, C.D., Muenow, D.W., Garcia, M.O., 1983. Volatiles in basalts and andesites from the Galapagos Spreading Center, 85° to 86°W. Geochim. Cosmochim. Acta 47, 1551–1558. https://doi.org/10.1016/0016-7037(83)90181-3

Cabral, R.A., Jackson, M.G., Koga, K.T., Rose-Koga, E.F., Hauri, E.H., Whitehouse, M.J., Price, A.A., Day, J.M.D., Shimizu, N., Kelley, K.A., 2014. Volatile cycling of H_2O, CO_2, F, and Cl in the HIMU mantle: A new window provided by melt inclusions from oceanic hot spot lavas at Mangaia, Cook Islands. Geochem. Geophys. Geosystems 15, 4445–4467. https://doi.org/10.1002/2014GC005473

Canales, J.P., Dunn, R.A., Ito, G., Detrick, R.S., Sallarès, V., 2014. Effect of Variations in Magma Supply on the Crustal Structure of Mid-Ocean Ridges: Insights from the Western Galápagos Spreading Center, in: Harpp, K.S., Mittelstaedt, E., d'Ozouville, N., Graham, D.W. (Eds.),

814 Geophysical Monograph Series. John Wiley & Sons, Inc, Hoboken, New Jersey, pp. 363–391.
815 https://doi.org/10.1002/9781118852538.ch17
816 Canales, J.P., Ito, G., Detrick, R.S., Sinton, J., 2002. Crustal thickness along the western Galápagos
817 Spreading Center and the compensation of the Galápagos hotspot swell. Earth Planet. Sci.
818 Lett. 203, 311–327. https://doi.org/10.1016/S0012-821X(02)00843-9
819 Christie, D.M., Werner, R., Hauff, F., Hoernle, K., Hanan, B.B., 2005. Morphological and geochemical
820 variations along the eastern Galápagos Spreading Center. Geochem. Geophys. Geosystems
821 6, n/a-n/a. https://doi.org/10.1029/2004GC000714
822 Cushman, B., Sinton, J., Ito, G., Eaby Dixon, J., 2004. Glass compositions, plume-ridge interaction, and
823 hydrous melting along the Galápagos Spreading Center, 90.5°W to 98°W. Geochem.
824 Geophys. Geosystems 5. https://doi.org/10.1029/2004GC000709
825 Dalou, C., Koga, K. T., Shimizu, N., 2012. Experimental determination of F and Cl partitioning
826 between lherzolite and basaltic melt. Contrib. Mineral. Petrol. 163, 591–609.
827 Danyushevsky, L.V., Eggins, S.M., Falloon, T.J., Christie, D.M., 2000. H2O Abundance in Depleted to
828 Moderately Enriched Mid-ocean Ridge Magmas; Part I: Incompatible Behaviour, Implications
829 for Mantle Storage, and Origin of Regional Variations. J. Petrol. 41, 1329–1364.
830 https://doi.org/10.1093/petrology/41.8.1329
831 Day, J.M.D., Barry, P.H., Hilton, D.R., Burgess, R., Pearson, D.G., Taylor, L.A., 2015. The helium flux
832 from the continents and ubiquity of low-3He/4He recycled crust and lithosphere. Geochim.
833 Cosmochim. Acta 153, 116–133. https://doi.org/10.1016/j.gca.2015.01.008
834 Detrick, R.S., Sinton, J.M., Ito, G., Canales, J.P., Behn, M., Blacic, T., Cushman, B., Dixon, J.E., Graham,
835 D.W., Mahoney, J.J., 2002. Correlated geophysical, geochemical, and volcanological
836 manifestations of plume-ridge interaction along the Galápagos Spreading Center. Geochem.
837 Geophys. Geosystems 3, 1–14. https://doi.org/10.1029/2002GC000350
838 Dixon, J.E., 1997. Degassing of alkalic basalts. Am. Mineral. 82, 368–378.
839 https://doi.org/10.2138/am-1997-3-415
840 Dixon, J.E., Bindeman, I.N., Kingsley, R.H., Simons, K.K., Le Roux, P.J., Hajewski, T.R., Swart, P.,
841 Langmuir, C.H., Ryan, J.G., Walowski, K.J., Wada, I., Wallace, P.J., 2017. Light Stable Isotopic
842 Compositions of Enriched Mantle Sources: Resolving the Dehydration Paradox. Geochem.
843 Geophys. Geosystems 18, 3801–3839. https://doi.org/10.1002/2016GC006743
844 Donnelly, K.E., Goldstein, S.L., Langmuir, C.H., Spiegelman, M., 2004. Origin of enriched ocean ridge
845 basalts and implications for mantle dynamics. Earth Planet. Sci. Lett. 226, 347–366.
846 https://doi.org/10.1016/j.epsl.2004.07.019
847 Farnetani, D.G., Richards, M.A., 1995. Thermal entrainment and melting in mantle plumes. Earth
848 Planet. Sci. Lett. 136, 251–267. https://doi.org/10.1016/0012-821X(95)00158-9
849 Geist, D., Naumann, T., Larson, P., 1998. Evolution of Galapagos Magmas: Mantle and Crustal
850 Fractionation without Assimilation. J. Petrol. 39, 953–971.
851 https://doi.org/10.1093/petroj/39.5.953
852 Gibson, S.A., Dale, C.W., Geist, D.J., Day, J.A., Brügmann, G., Harpp, K.S., 2016. The influence of melt
853 flux and crustal processing on Re–Os isotope systematics of ocean island basalts: Constraints
854 from Galápagos. Earth Planet. Sci. Lett. 449, 345–359.
855 https://doi.org/10.1016/j.epsl.2016.05.021
856 Gibson, S.A., Geist, D., 2010. Geochemical and geophysical estimates of lithospheric thickness
857 variation beneath Galápagos. Earth Planet. Sci. Lett. 300, 275–286.
858 https://doi.org/10.1016/j.epsl.2010.10.002
859 Gibson, S.A., Geist, D.J., Richards, M.A., 2015. Mantle plume capture, anchoring, and outflow during
860 Galápagos plume-ridge interaction: Mantle plume capture & outflow. Geochem. Geophys.
861 Geosystems 16, 1634–1655. https://doi.org/10.1002/2015GC005723
862 Gibson, S.A., Richards, M.A., 2018. Delivery of deep-sourced, volatile-rich plume material to the
863 global ridge system. Earth Planet. Sci. Lett. 499, 205–218.
864 https://doi.org/10.1016/j.epsl.2018.07.028

Gibson, S.A., Rooks, E.E., Day, J.A., Petrone, C.M., Leat, P.T., 2020. The role of sub-continental mantle as both "sink" and "source" in deep Earth volatile cycles. Geochim. Cosmochim. Acta 275, 140–162. https://doi.org/10.1016/j.gca.2020.02.018

Gleeson, M., Soderman, C., Matthews, S., Cottaar, S., and Gibson, S., 2021. Geochemical constraints on the structure of the Earth's deep mantle and the origin of the LLSVPs (preprint). Earth Sciences. https://doi.org/10.31223/X57P5C

Gleeson, M.L.M., Gibson, S.A., 2019. Crustal controls on apparent mantle pyroxenite signals in ocean-island basalts. Geology. https://doi.org/10.1130/G45759.1

Gleeson, M.L.M., Gibson, S.A., Williams, H.M., 2020. Novel insights from Fe-isotopes into the lithological heterogeneity of Ocean Island Basalts and plume-influenced MORBs. Earth Planet. Sci. Lett. 535, 116114. https://doi.org/10.1016/j.epsl.2020.116114

Graham, D.W., Hanan, B.B., Lupton, J.E., Hoernle, K., Werner, R., Christie, D.M., Sinton, J.M., 2014. Helium Isotope Variations and Mantle Plume-Spreading Ridge Interactions Along the Galápagos Spreading Center, in: Harpp, K.S., Mittelstaedt, E., d'Ozouville, N., Graham, D.W. (Eds.), Geophysical Monograph Series. John Wiley & Sons, Inc, Hoboken, New Jersey, pp. 393–414. https://doi.org/10.1002/9781118852538.ch18

Hanan, B.B., Graham, D.W., 1996. Lead and Helium Isotope Evidence from Oceanic Basalts for a Common Deep Source of Mantle Plumes. Science 272, 991–995. https://doi.org/10.1126/science.272.5264.991

Harpp, K.S., Geist, D.J., Koleszar, A.M., Christensen, B., Lyons, J., Sabga, M., Rollins, N., 2014a. The Geology and Geochemistry of Isla Floreana, Galápagos: A Different Type of Late-Stage Ocean Island Volcanism, in: Harpp, K.S., Mittelstaedt, E., d'Ozouville, N., Graham, D.W. (Eds.), Geophysical Monograph Series. John Wiley & Sons, Inc, Hoboken, New Jersey, pp. 71–117. https://doi.org/10.1002/9781118852538.ch6

Harpp, K.S., Hall, P.S., Jackson, M.G., 2014b. Galápagos and Easter: A Tale of Two Hotspots, in: Harpp, K.S., Mittelstaedt, E., d'Ozouville, N., Graham, D.W. (Eds.), Geophysical Monograph Series. John Wiley & Sons, Inc, Hoboken, New Jersey, pp. 27–40. https://doi.org/10.1002/9781118852538.ch3

Harpp, K.S., Weis, D., 2020. Insights Into the Origins and Compositions of Mantle Plumes: A Comparison of Galápagos and Hawai'i. Geochem. Geophys. Geosystems 21. https://doi.org/10.1029/2019GC008887

Harpp, K.S., White, W.M., 2001. Tracing a mantle plume: Isotopic and trace element variations of Galápagos seamounts. Geochem. Geophys. Geosystems 2. https://doi.org/10.1029/2000GC000137

Harpp, K.S., Wirth, K.R., Teasdale, R., Blair, S., Reed, L., Barr, J., Pistiner, J., Korich, D., 2014c. Plume-Ridge Interaction in the Galápagos: Perspectives from Wolf, Darwin, and Genovesa Islands, in: Harpp, K.S., Mittelstaedt, E., d'Ozouville, N., Graham, D.W. (Eds.), Geophysical Monograph Series. John Wiley & Sons, Inc, Hoboken, New Jersey, pp. 285–334. https://doi.org/10.1002/9781118852538.ch15

Hart, S.R., Hauri, E.H., Oschmann, L.A., Whitehead, J.A., 1992. Mantle Plumes and Entrainment: Isotopic Evidence. Science 256, 517–520. https://doi.org/10.1126/science.256.5056.517

Hauri, E., Gaetani, G., Green, T., 2006. Partitioning of water during melting of the Earth's upper mantle at H2O-undersaturated conditions. Earth Planet. Sci. Lett. 248, 715–734. https://doi.org/10.1016/j.epsl.2006.06.014

Herzberg, C., Asimow, P.D., 2008. Petrology of some oceanic island basalts: PRIMELT2.XLS software for primary magma calculation. Geochem. Geophys. Geosystems 9, n/a-n/a. https://doi.org/10.1029/2008GC002057

Hirth, G., Kohlstedt, D., 2003. Rheology of the upper mantle and the mantle wedge: A view from the experimentalists, in: Eiler, J. (Ed.), Geophysical Monograph Series. American Geophysical Union, Washington, D. C., pp. 83–105. https://doi.org/10.1029/138GM06

915 Hirth, G., Kohlstedt, D.L., 1996. Water in the oceanic upper mantle: implications for rheology, melt
916 extraction and the evolution of the lithosphere. Earth Planet. Sci. Lett. 144, 93–108.
917 https://doi.org/10.1016/0012-821X(96)00154-9
918 Hoernle, K., Werner, R., Morgan, J.P., Garbe-Schönberg, D., Bryce, J., Mrazek, J., 2000. Existence of
919 complex spatial zonation in the Galápagos plume. Geology 28, 435.
920 https://doi.org/10.1130/0091-7613(2000)28<435:EOCSZI>2.0.CO;2
921 Hooft, E.E.E., Toomey, D.R., Solomon, S.C., 2003. Anomalously thin transition zone beneath the
922 Galápagos hotspot. Earth Planet. Sci. Lett. 216, 55–64. https://doi.org/10.1016/S0012-
923 821X(03)00517-X
924 Iacovino, K., Matthews, S., Wieser, P., Moore, G., Bégué, F., 2020. VESIcal Part I: An open-source
925 thermodynamic model engine for mixed volatile (H2O-CO2) solubility in silicate melts
926 (preprint). Earth Sciences. https://doi.org/10.31223/X5D606
927 Ingle, S., Ito, G., Mahoney, J.J., Chazey, W., Sinton, J., Rotella, M., Christie, D.M., 2010. Mechanisms
928 of geochemical and geophysical variations along the western Galápagos Spreading Center.
929 Geochem. Geophys. Geosystems 11, n/a-n/a. https://doi.org/10.1029/2009GC002694
930 Ito, G., Bianco, T., 2014. Patterns in Galápagos Magmatism Arising from the Upper Mantle Dynamics
931 of Plume-Ridge Interaction, in: Harpp, K.S., Mittelstaedt, E., d'Ozouville, N., Graham, D.W.
932 (Eds.), Geophysical Monograph Series. John Wiley & Sons, Inc, Hoboken, New Jersey, pp.
933 245–261. https://doi.org/10.1002/9781118852538.ch13
934 Ito, G., Lin, J., 1995. Oceanic spreading center–hotspot interactions: Constraints from along-isochron
935 bathymetric and gravity anomalies. Geology 23, 657. https://doi.org/10.1130/0091-
936 7613(1995)023<0657:OSCHIC>2.3.CO;2
937 Ito, G., Lin, J., Gable, C.W., 1997. Interaction of mantle plumes and migrating mid-ocean ridges:
938 Implications for the Galápagos plume-ridge system. J. Geophys. Res. Solid Earth 102, 15403–
939 15417. https://doi.org/10.1029/97JB01049
940 Ito, G., Lin, J., Graham, D.W., 2003. Observational and theoretical studies of the dynamics of mantle
941 plume–mid-ocean ridge interaction. Rev. Geophys. 41.
942 https://doi.org/10.1029/2002RG000117
943 Ito, G., Mahoney, J.J., 2005. Flow and melting of a heterogeneous mantle: 1. Method and
944 importance to the geochemistry of ocean island and mid-ocean ridge basalts. Earth Planet.
945 Sci. Lett. 230, 29–46. https://doi.org/10.1016/j.epsl.2004.10.035
946 Jackson, M.G., Koga, K.T., Price, A., Konter, J.G., Koppers, A.A.P., Finlayson, V.A., Konrad, K., Hauri,
947 E.H., Kylander-Clark, A., Kelley, K.A., Kendrick, M.A., 2015. Deeply dredged submarine HIMU
948 glasses from the Tuvalu Islands, Polynesia: Implications for volatile budgets of recycled
949 oceanic crust. Geochem. Geophys. Geosystems 16, 3210–3234.
950 https://doi.org/10.1002/2015GC005966
951 Jarosewich, E., Nelen, J.A., Norberg, J.A., 1980. Reference Samples for Electron Microprobe
952 Analysis*. Geostand. Geoanalytical Res. 4, 43–47. https://doi.org/10.1111/j.1751-
953 908X.1980.tb00273.x
954 Johnson, E.A., 2006. 6. Water in Nominally Anhydrous Crustal Minerals: Speciation, Concentration,
955 and Geologic Significance, in: Keppler, H., Smyth, J.R. (Eds.), Water in Nominally Anhydrous
956 Minerals. De Gruyter, Berlin, Boston, pp. 117–154. https://doi.org/10.1515/9781501509476-
957 010
958 Katz, R.F., Spiegelman, M., Langmuir, C.H., 2003. A new parameterization of hydrous mantle melting.
959 Geochem. Geophys. Geosystems 4, n/a-n/a. https://doi.org/10.1029/2002GC000433
960 Katz, R.F., Weatherley, S.M., 2012. Consequences of mantle heterogeneity for melt extraction at
961 mid-ocean ridges. Earth Planet. Sci. Lett. 335–336, 226–237.
962 https://doi.org/10.1016/j.epsl.2012.04.042
963 Kelemen, P.B., Hirth, G., Shimizu, N., Spiegelman, M., Dick, H.J., 1997. A review of melt migration
964 processes in the adiabatically upwelling mantle beneath oceanic spreading ridges. Philos.

965 Trans. R. Soc. Lond. Ser. Math. Phys. Eng. Sci. 355, 283–318.
966 https://doi.org/10.1098/rsta.1997.0010
967 Keller, T., Katz, R.F., 2016. The Role of Volatiles in Reactive Melt Transport in the Asthenosphere. J.
968 Petrol. 57, 1073–1108. https://doi.org/10.1093/petrology/egw030
969 Kendrick, M.A., Hémond, C., Kamenetsky, V.S., Danyushevsky, L., Devey, C.W., Rodemann, T.,
970 Jackson, M.G., Perfit, M.R., 2017. Seawater cycled throughout Earth's mantle in partially
971 serpentinized lithosphere. Nat. Geosci. 10, 222–228. https://doi.org/10.1038/ngeo2902
972 Kendrick, M.A., Jackson, M.G., Hauri, E.H., Phillips, D., 2015. The halogen (F, Cl, Br, I) and H2O
973 systematics of Samoan lavas: Assimilated-seawater, EM2 and high-3He/4He components.
974 Earth Planet. Sci. Lett. 410, 197–209. https://doi.org/10.1016/j.epsl.2014.11.026
975 Kingsley, R.H., Schilling, J.-G., 1998. Plume-ridge interaction in the Easter-Salas y Gomez seamount
976 chain-Easter Microplate system: Pb isotope evidence. J. Geophys. Res. Solid Earth 103,
977 24159–24177. https://doi.org/10.1029/98JB01496
978 Kokfelt, T., Lundstrom, C., Hoernle, K., Hauff, F., Werner, R., 2005. Plume–ridge interaction studied
979 at the Galápagos spreading center: Evidence from 226Ra–230Th–238U and 231Pa–235U
980 isotopic disequilibria. Earth Planet. Sci. Lett. 234, 165–187.
981 https://doi.org/10.1016/j.epsl.2005.02.031
982 Koleszar, A.M., Saal, A.E., Hauri, E.H., Nagle, A.N., Liang, Y., Kurz, M.D., 2009. The volatile contents of
983 the Galapagos plume; evidence for H2O and F open system behavior in melt inclusions.
984 Earth Planet. Sci. Lett. 287, 442–452. https://doi.org/10.1016/j.epsl.2009.08.029
985 Kurz, M.D., Curtice, J., Fornari, D., Geist, D., Moreira, M., 2009. Primitive neon from the center of the
986 Galápagos hotspot. Earth Planet. Sci. Lett. 286, 23–34.
987 https://doi.org/10.1016/j.epsl.2009.06.008
988 Kurz, M.D., Geist, D., 1999. Dynamics of the Galapagos hotspot from helium isotope geochemistry.
989 Geochim. Cosmochim. Acta 63, 4139–4156. https://doi.org/10.1016/S0016-7037(99)00314-
990 2
991 Lambart, S., 2017. No direct contribution of recycled crust in Icelandic basalts. Geochem. Perspect.
992 Lett. 7–12. https://doi.org/10.7185/geochemlet.1728
993 Langmuir, C.H., Bender, J.F., 1984. The geochemistry of oceanic basalts in the vicinity of transform
994 faults: Observations and implications. Earth Planet. Sci. Lett. 69, 107–127.
995 https://doi.org/10.1016/0012-821X(84)90077-3
996 Le Roux, P., Shirey, S., Hauri, E., Perfit, M., Bender, J., 2006. The effects of variable sources,
997 processes and contaminants on the composition of northern EPR MORB (8–10°N and 12–
998 14°N): Evidence from volatiles (H2O, CO2, S) and halogens (F, Cl). Earth Planet. Sci. Lett. 251,
999 209–231. https://doi.org/10.1016/j.epsl.2006.09.012
1000 Le Voyer, M., Cottrell, E., Kelley, K.A., Brounce, M., Hauri, E.H., 2015. The effect of primary versus
1001 secondary processes on the volatile content of MORB glasses: An example from the
1002 equatorial Mid-Atlantic Ridge (5°N-3°S): MORB volatile contents along 5°N-3°S MAR. J.
1003 Geophys. Res. Solid Earth 120, 125–144. https://doi.org/10.1002/2014JB011160
1004 Le Voyer, M., Hauri, E.H., Cottrell, E., Kelley, K.A., Salters, V.J.M., Langmuir, C.H., Hilton, D.R., Barry,
1005 P.H., Füri, E., 2018. Carbon fluxes and primary magma CO_2 contents along the global mid-
1006 ocean ridge system. Geochem. Geophys. Geosystems.
1007 https://doi.org/10.1029/2018GC007630
1008 Maclennan, J., McKenzie, D., Gronvöld, K., 2001. Plume-driven upwelling under central Iceland. Earth
1009 Planet. Sci. Lett. 194, 67–82. https://doi.org/10.1016/S0012-821X(01)00553-2
1010 Marks, M.A.W., Kendrick, M.A., Eby, G.N., Zack, T., Wenzel, T., 2017. The F, Cl, Br and I Contents of
1011 Reference Glasses BHVO-2G, BIR-1G, BCR-2G, GSD-1G, GSE-1G, NIST SRM 610 and NIST SRM
1012 612. Geostand. Geoanalytical Res. 41, 107–122. https://doi.org/10.1111/ggr.12128
1013 Matthews, S., Shorttle, O., Wong, K., 2020. simonwmatthews/pyMelt: First Release. Zenodo.
1014 https://doi.org/10.5281/ZENODO.4011814

Métrich, N., Zanon, V., Créon, L., Hildenbrand, A., Moreira, M., Marques, F.O., 2014. Is the 'Azores Hotspot' a Wetspot? Insights from the Geochemistry of Fluid and Melt Inclusions in Olivine of Pico Basalts. J. Petrol. 55, 377–393. https://doi.org/10.1093/petrology/egt071

Michael, P., 1995. Regionally distinctive sources of depleted MORB: Evidence from trace elements and H2O. Earth Planet. Sci. Lett. 131, 301–320. https://doi.org/10.1016/0012-821X(95)00023-6

Michael, P.J., 1999. Implications for magmatic processes at Ontong Java Plateau from volatile and major element contents of Cretaceous basalt glasses. Geochem Geophys Geosyst 1.

Michael, P.J., 1988. The concentration, behavior and storage of H2O in the suboceanic upper mantle: Implications for mantle metasomatism. Geochim. Cosmochim. Acta 52, 555–566. https://doi.org/10.1016/0016-7037(88)90110-X

Michael, P.J., Cornell, W.C., 1998. Influence of spreading rate and magma supply on crystallization and assimilation beneath mid-ocean ridges: Evidence from chlorine and major element chemistry of mid-ocean ridge basalts. J. Geophys. Res. Solid Earth 103, 18325–18356. https://doi.org/10.1029/98JB00791

Mittal, T., Richards, M.A., 2017. Plume-ridge interaction via melt channelization at Galápagos and other near-ridge hotspot provinces. Geochem. Geophys. Geosystems 18, 1711–1738. https://doi.org/10.1002/2016GC006454

Mittelstaedt, E., Soule, A.S., Harpp, K.S., Fornari, D., 2014. Variations in Crustal Thickness, Plate Rigidity, and Volcanic Processes Throughout the Northern Galápagos Volcanic Province, in: Harpp, K.S., Mittelstaedt, E., d'Ozouville, N., Graham, D.W. (Eds.), Geophysical Monograph Series. John Wiley & Sons, Inc, Hoboken, New Jersey, pp. 263–284. https://doi.org/10.1002/9781118852538.ch14

Morgan, W.J., 1978. Rodriguez, Darwin, Amsterdam, ..., A second type of Hotspot Island. J. Geophys. Res. 83, 5355. https://doi.org/10.1029/JB083iB11p05355

Morgan, W.J., 1971. Convection Plumes in the Lower Mantle. Nature 230, 42–43. https://doi.org/10.1038/230042a0

Peterson, M.E., Saal, A.E., Kurz, M.D., Hauri, E.H., Blusztajn, J.S., Harpp, K.S., Werner, R., Geist, D.J., 2017. Submarine Basaltic Glasses from the Galapagos Archipelago: Determining the Volatile Budget of the Mantle Plume. J. Petrol. 58, 1419–1450. https://doi.org/10.1093/petrology/egx059

Reekie, C.D.J., Jenner, F.E., Smythe, D.J., Hauri, E.H., Bullock, E.S., Williams, H.M., 2019. Sulfide resorption during crustal ascent and degassing of oceanic plateau basalts. Nat. Commun. 10. https://doi.org/10.1038/s41467-018-08001-3

Ribe, N.M., 1996. The dynamics of plume-ridge interaction: 2. Off-ridge plumes. J. Geophys. Res. Solid Earth 101, 16195–16204. https://doi.org/10.1029/96JB01187

Rosenthal, A., Hauri, E.H., Hirschmann, M.M., 2015. Experimental determination of C, F, and H partitioning between mantle minerals and carbonated basalt, CO 2 /Ba and CO 2 /Nb systematics of partial melting, and the CO 2 contents of basaltic source regions. Earth Planet. Sci. Lett. 412, 77–87. https://doi.org/10.1016/j.epsl.2014.11.044

Ryan, W.B.F., Carbotte, S.M., Coplan, J.O., O'Hara, S., Melkonian, A., Arko, R., Weissel, R.A., Ferrini, V., Goodwillie, A., Nitsche, F., Bonczkowski, J., Zemsky, R., 2009. Global Multi-Resolution Topography synthesis. Geochem. Geophys. Geosystems 10, n/a-n/a. https://doi.org/10.1029/2008GC002332

Saal, A.E., Hauri, E.H., Langmuir, C.H., Perfit, M.R., 2002. Vapour undersaturation in primitive mid-ocean-ridge basalt and the volatile content of Earth's upper mantle. Nature 419, 451–455. https://doi.org/10.1038/nature01073

Salters, V.J.M., Stracke, A., 2004. Composition of the depleted mantle. Geochem. Geophys. Geosystems 5, n/a-n/a. https://doi.org/10.1029/2003GC000597

1064 Schilling, J.-G., 1991. Fluxes and excess temperatures of mantle plumes inferred from their
1065 interaction with migrating mid-ocean ridges. Nature 352, 397–403.
1066 https://doi.org/10.1038/352397a0
1067 Schilling, J.-G., Fontignie, D., Blichert-Toft, J., Kingsley, R., Tomza, U., 2003. Pb-Hf-Nd-Sr isotope
1068 variations along the Galápagos Spreading Center (101°-83°W): Constraints on the dispersal
1069 of the Galápagos mantle plume. Geochem. Geophys. Geosystems 4.
1070 https://doi.org/10.1029/2002GC000495
1071 Schilling, J.-G., Kingsley, R.H., Devine, J.D., 1982. Galapagos Hot Spot-Spreading Center System: 1.
1072 Spatial petrological and geochemical variations (83°W-101°W). J. Geophys. Res. Solid Earth
1073 87, 5593–5610. https://doi.org/10.1029/JB087iB07p05593
1074 Shimizu, K., Ito, M., Chang, Q., Miyazaki, T., Ueki, K., Toyama, C., Senda, R., Vaglarov, B.S., Ishikawa,
1075 T., Kimura, J.-I., 2019. Identifying volatile mantle trend with the water–fluorine–cerium
1076 systematics of basaltic glass. Chem. Geol. 522, 283–294.
1077 https://doi.org/10.1016/j.chemgeo.2019.06.014
1078 Shimizu, K., Saal, A.E., Myers, C.E., Nagle, A.N., Hauri, E.H., Forsyth, D.W., Kamenetsky, V.S., Niu, Y.,
1079 2016. Two-component mantle melting-mixing model for the generation of mid-ocean ridge
1080 basalts: Implications for the volatile content of the Pacific upper mantle. Geochim.
1081 Cosmochim. Acta 176, 44–80. https://doi.org/10.1016/j.gca.2015.10.033
1082 Shishkina, T.A., Botcharnikov, R.E., Holtz, F., Almeev, R.R., Jazwa, A.M., Jakubiak, A.A., 2014.
1083 Compositional and pressure effects on the solubility of H2O and CO2 in mafic melts. Chem.
1084 Geol. 388, 112–129. https://doi.org/10.1016/j.chemgeo.2014.09.001
1085 Shishkina, T.A., Botcharnikov, R.E., Holtz, F., Almeev, R.R., Portnyagin, M.V., 2010. Solubility of H2O-
1086 and CO2-bearing fluids in tholeiitic basalts at pressures up to 500MPa. Chem. Geol. 277,
1087 115–125. https://doi.org/10.1016/j.chemgeo.2010.07.014
1088 Shorttle, O., Maclennan, J., Jones, S.M., 2010. Control of the symmetry of plume-ridge interaction by
1089 spreading ridge geometry. Geochem. Geophys. Geosystems 11, n/a-n/a.
1090 https://doi.org/10.1029/2009GC002986
1091 Sinton, J., Detrick, R., Canales, J.P., Ito, G., Behn, M., 2003. Morphology and segmentation of the
1092 western Galápagos Spreading Center, 90.5°-98°W: Plume-ridge interaction at an
1093 intermediate spreading ridge. Geochem. Geophys. Geosystems 4.
1094 https://doi.org/10.1029/2003GC000609
1095 Sinton, J.M., Detrick, R.S., 1992. Mid-ocean ridge magma chambers. J. Geophys. Res. 97, 197.
1096 https://doi.org/10.1029/91JB02508
1097 Sleep, N.H., 1990. Hotspots and mantle plumes: Some phenomenology. J. Geophys. Res. 95, 6715.
1098 https://doi.org/10.1029/JB095iB05p06715
1099 Sobolev, A.V., Hofmann, A.W., Kuzmin, D.V., Yaxley, G.M., Arndt, N.T., Chung, S.-L., Danyushevsky,
1100 L.V., Elliott, T., Frey, F.A., Garcia, M.O., Gurenko, A.A., Kamenetsky, V.S., Kerr, A.C.,
1101 Krivolutskaya, N.A., Matvienkov, V.V., Nikogosian, I.K., Rocholl, A., Sigurdsson, I.A.,
1102 Sushchevskaya, N.M., Teklay, M., 2007. The Amount of Recycled Crust in Sources of Mantle-
1103 Derived Melts 316, 7.
1104 Sorbadere, F., Médard, E., Laporte, D., Schiano, P., 2013. Experimental melting of hydrous
1105 peridotite–pyroxenite mixed sources: Constraints on the genesis of silica-undersaturated
1106 magmas beneath volcanic arcs. Earth Planet. Sci. Lett. 15.
1107 Stroncik, N.A., Devey, C.W., 2011. Recycled gabbro signature in hotspot magmas unveiled by plume–
1108 ridge interactions. Nat. Geosci. 4, 393–397. https://doi.org/10.1038/ngeo1121
1109 Stroncik, N.A., Niedermann, S., Haase, K.M., 2008. Plume–ridge interaction revisited: Evidence for
1110 melt mixing from He, Ne and Ar isotope and abundance systematics. Earth Planet. Sci. Lett.
1111 268, 424–432. https://doi.org/10.1016/j.epsl.2008.01.037
1112 Sun, Z., Xiong, X., Wang, J., Liu, X., Li, L., Ruan, M., Zhang, L., Takahashi, E., 2020. Sulfur abundance
1113 and heterogeneity in the MORB mantle estimated by copper partitioning and sulfur

solubility modelling. Earth Planet. Sci. Lett. 538, 116169. https://doi.org/10.1016/j.epsl.2020.116169

Verma, S.P., Schilling, J.-G., 1982. Galapagos Hot Spot-SPreading Center System: 2. ^{87}SR/^{86}SR and large ion lithophile element variations (85°W-101°W). J. Geophys. Res. Solid Earth 87, 10838–10856. https://doi.org/10.1029/JB087iB13p10838

Vidito, C., Herzberg, C., Gazel, E., Geist, D., Harpp, K., 2013. Lithological structure of the Galápagos Plume: Lithological Structure Galpagos Plume. Geochem. Geophys. Geosystems 14, 4214–4240. https://doi.org/10.1002/ggge.20270

Villagómez, D.R., Toomey, D.R., Geist, D.J., Hooft, E.E.E., Solomon, S.C., 2014. Mantle flow and multistage melting beneath the Galápagos hotspot revealed by seismic imaging. Nat. Geosci. 7, 151–156. https://doi.org/10.1038/ngeo2062

Weatherley, S.M., Katz, R.F., 2012. Melting and channelized magmatic flow in chemically heterogeneous, upwelling mantle. Geochem. Geophys. Geosystems 13. https://doi.org/10.1029/2011GC003989

Weatherley, S.M., Katz, R.F., 2010. Plate-driven mantle dynamics and global patterns of mid-ocean ridge bathymetry. Geochem. Geophys. Geosystems 11, n/a-n/a. https://doi.org/10.1029/2010GC003192

Weis, D., Garcia, M.O., Rhodes, J.M., Jellinek, M., Scoates, J.S., 2011. Role of the deep mantle in generating the compositional asymmetry of the Hawaiian mantle plume. Nat. Geosci. 4, 831–838. https://doi.org/10.1038/ngeo1328

White, W.M., McBirney, A.R., Duncan, R.A., 1993. Petrology and geochemistry of the Galápagos Islands: Portrait of a pathological mantle plume. J. Geophys. Res. Solid Earth 98, 19533–19563. https://doi.org/10.1029/93JB02018

Wieser, P.E., Jenner, F., Edmonds, M., Maclennan, J., Kunz, B.E., 2020. Chalcophile elements track the fate of sulfur at Kīlauea Volcano, Hawai'i. Geochim. Cosmochim. Acta S0016703720303239. https://doi.org/10.1016/j.gca.2020.05.018

Workman, R.K., Hart, S.R., 2005. Major and trace element composition of the depleted MORB mantle (DMM). Earth Planet. Sci. Lett. 231, 53–72. https://doi.org/10.1016/j.epsl.2004.12.005

Workman, R.K., Hauri, E., Hart, S.R., Wang, J., Blusztajn, J., 2006. Volatile and trace elements in basaltic glasses from Samoa: Implications for water distribution in the mantle. Earth Planet. Sci. Lett. 241, 932–951. https://doi.org/10.1016/j.epsl.2005.10.028

FIGURES

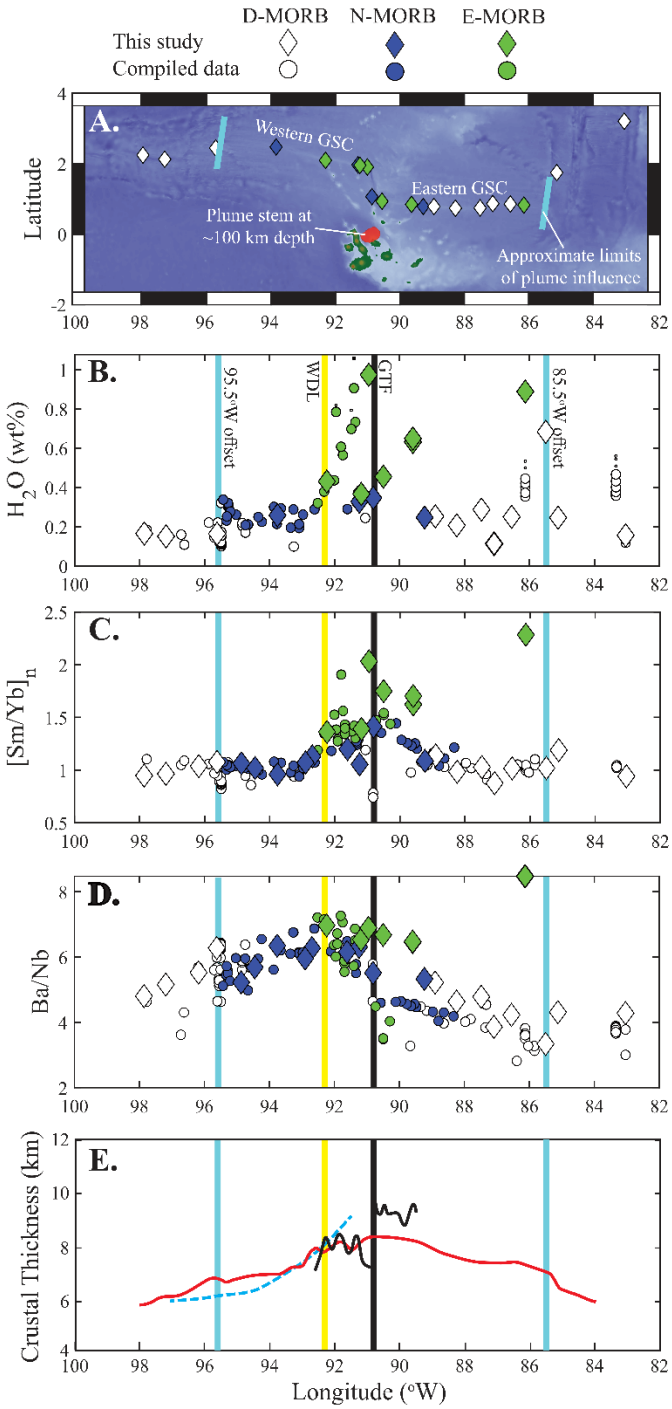

Figure 1 – Location and chemistry of the basalts from the GSC. **A.** Map of the Galápagos Spreading Centre (GSC) and Galápagos Archipelago (bathymetric data from Ryan et al., 2009). **B.** Brine-assimilation corrected H_2O contents in the GSC basalts from this study (diamonds) and from Cushman et al. (2004) and Le Voyer et al. (2018; circles). The measured H_2O contents of these

basalts are shown by the small dots (only visible where large differences between the measured and corrected H_2O concentrations are seen; Supplementary Information). Panels **C.** and **D.** show key trace element ratios ($[Sm/Yb]_n$ and Ba/Nb, respectively), which display an increased contribution from melts of a garnet-bearing lithology near the Galápagos Transform Fault (GTF; **C.**); and a geochemical offset between the western and eastern GSC, which relates to the incorporation of the Wolf-Darwin component in the mantle beneath the western GSC (**D.;** data from Christie et al., 2005; Gleeson et al., 2020; Ingle et al., 2010). Crustal thickness estimates are shown in panel **E.** from Ito and Lin (1995; red), Canales et al. (2002; blue), and Mittelstaedt et al. (2014; black). 2σ error is smaller than the symbol size for all graphs. Yellow line represents the intersection of the Wolf-Darwin Lineament with the GSC. The blue lines represent the approximate limit of plume influence along the GSC.

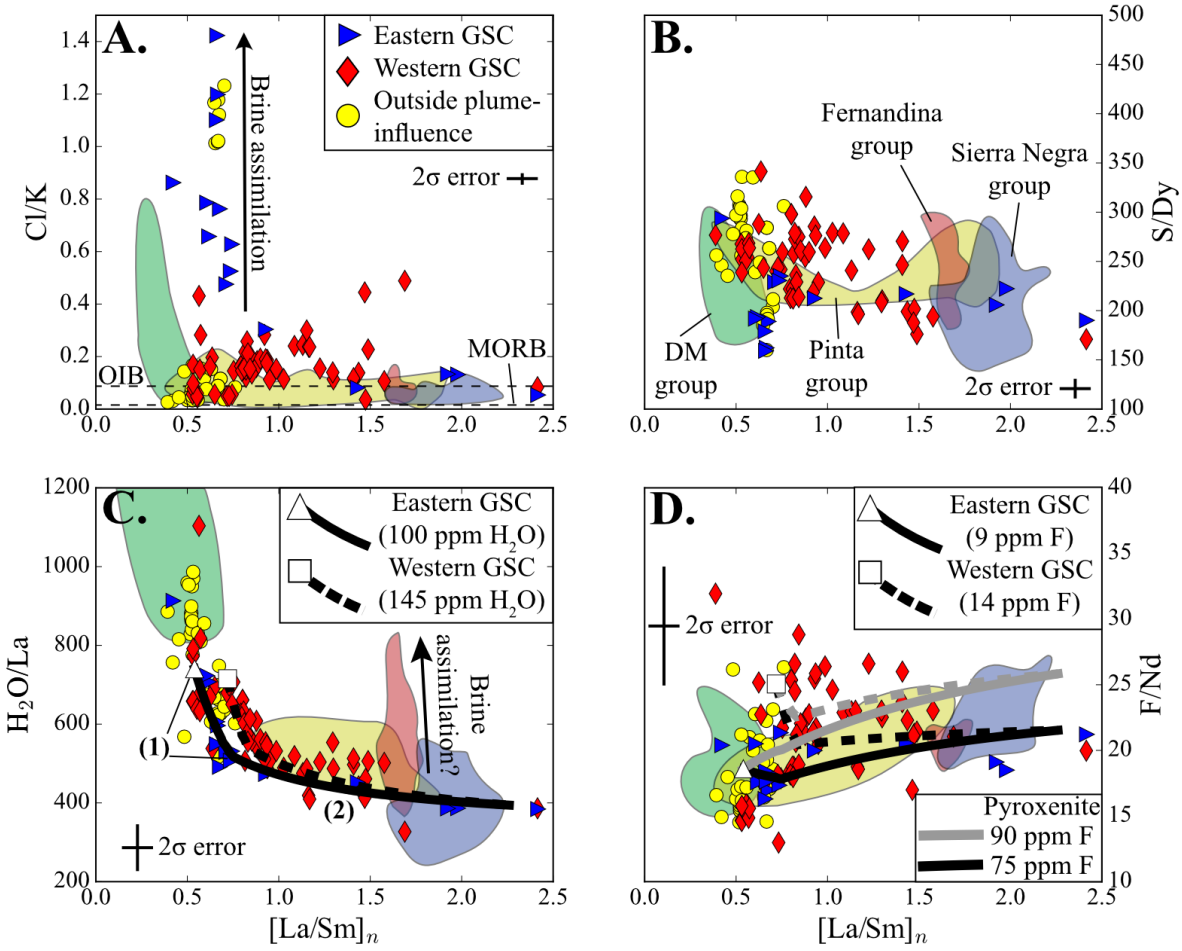

1164

Figure 2 – Relationship between volatile to non-volatile trace element ratios (e.g. H_2O/La) and indices of enrichment (represented here by $[La/Sm]_n$). Shown in all panels are the composition of the GSC basalts (colour coded according to location) as well as the composition of submarine basalts from the Galápagos Archipelago measured by Peterson et al. (2017). **A.** Many of the GSC basalts contain higher Cl/K ratios than those typically seen in MORBs or OIBs. Fernandina melt inclusions have Cl/K ratios of ~0.038 (Koleszar et al. 2009). **B.** The S/Dy ratios of GSC basalts are similar to those observed in basaltic glass chips from across the archipelago (Peterson et al., 2017). **C.** The H_2O/La ratio of plume-influenced GSC basalts varies from ~750 in depleted samples to <400 in the enriched samples. The white symbols and black lines show the compositions predicted by mantle melting models in this study. In the region labelled **(1)**, the black lines display the influence of increasing the amount of pyroxenitic material in the mantle source beneath the GSC (up to 8%, consistent with the models shown in Fig. 5). Region **(2)** displays the influence of increasing the contribution of channelised, plume-derived melts from a pyroxenitic source with ~550 ppm H_2O. The H_2O data from the GSC has been corrected for the influence of brine assimilation whereas the data for the submarine basalts from Peterson et al. (2017) has not (as different correction factors are required for each dataset). **D.** Black lines show the model predictions for increasing contribution of channelised flow where the enriched mantle end-member contains 75 ppm F. Grey lines show equivalent models for a scenario where the enriched, pyroxenitic end-member contains 90 ppm F. GSC data taken from this study (eastern GSC), Ingle et al. (2010), Cushman et al. (2004) and Le Voyer et al. (2018).

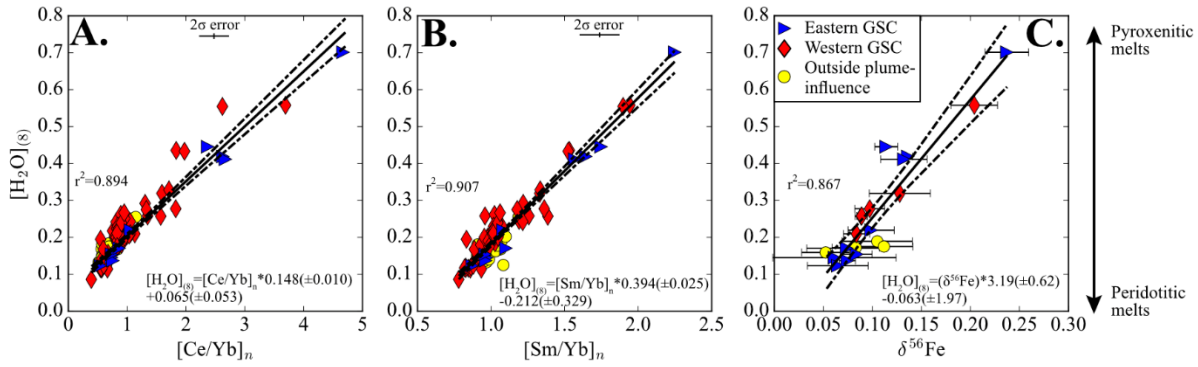

1185

1186 **Figure 3 –** Relationship between $[H_2O]_{(8)}$ and key geochemical indices of compositional enrichment.

1187 **A.** and **B.** display the correlation between trace element proxies of geochemical enrichment/melt

1188 fraction and $[H_2O]_{(8)}$ (fractionation corrected H_2O). The correlation between $[Sm/Yb]_n$ and $[H_2O]_{(8)}$

1189 (**A.**) is used to predict the fractionation corrected H_2O concentration of the GSC basalts for which

1190 volatile data does not exist. The data displayed here has been corrected for the influence of brine

1191 assimilation (Supplementary Information). **C.** A strong correlation is observed between $\delta^{56}Fe$ and

1192 $[H_2O]_{(8)}$, which indicates that there is a contribution of volatile-rich, pyroxenitic melts to the GSC

1193 basalts. Fe-isotope data from Gleeson et al. (2020), trace element and volatile element data from

1194 this study; Cushman et al. (2004); Gleeson et al. (2020); Ingle et al. (2010); and Le Voyer et al. (2018).

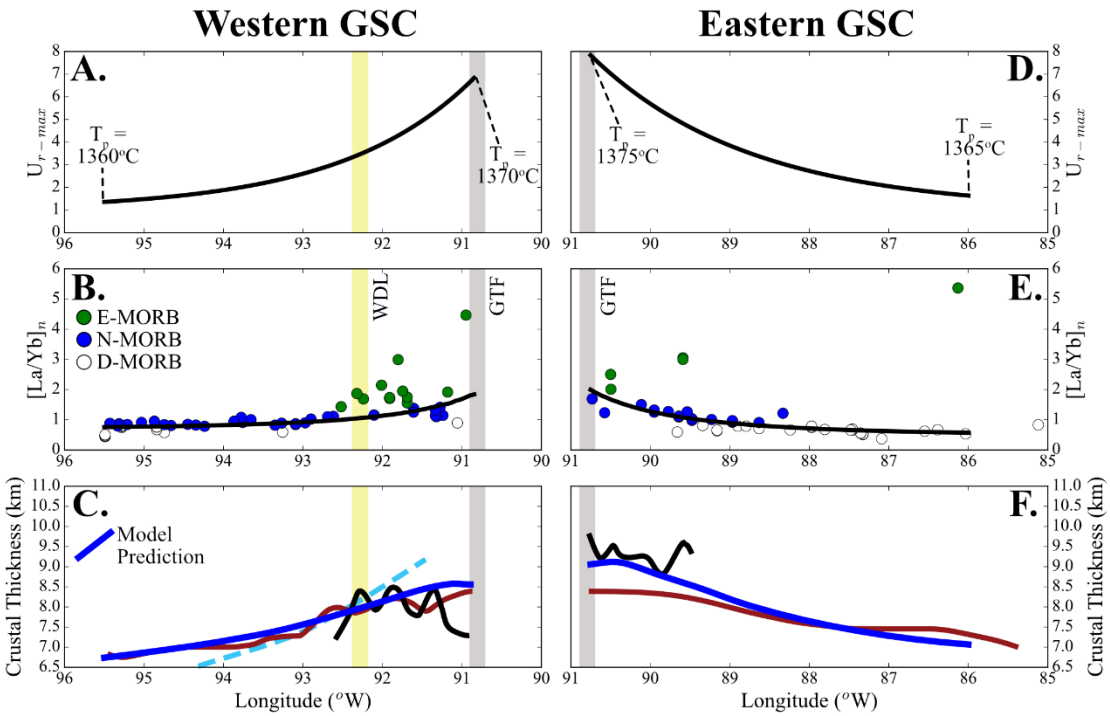

Figure 4 – Results of plume-ridge interaction models that only account for solid-state transport between the Galápagos mantle plume and the GSC. Panels **A. - C.** show the results for the western GSC and panels **D. - F.** show the results for the eastern GSC. Panels **A.** and **D.** show the input parameters for these models, and the geochemical (**B.** and **E.**) and crustal thickness (**C.** and **F.**) results are shown below. Black lines in **B.** and **E.** display the mean composition of melts delivered to that section of ridge. Crustal thickness estimates are from Ito and Lin (1995; red), Canales et al. (2002; blue), and Mittelstaedt et al. (2014; black); modelled crustal thickness is shown in blue (solid line). Some of the long length-scale trends in geochemical enrichment are reproduced along the GSC; however, several discrepancies can be observed between the model predictions and the crustal thickness and geochemical data from the GSC.

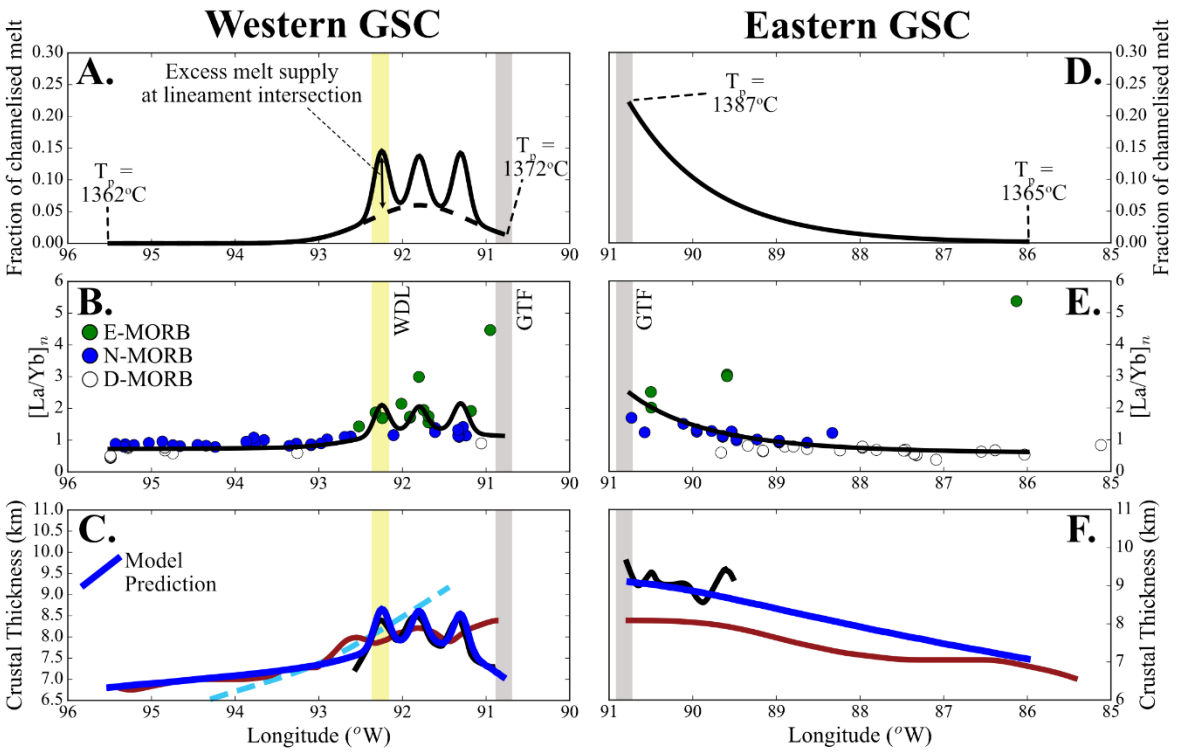

Figure 5 - Results of plume-ridge interaction models that account for channelised melt transport between the Galápagos mantle plume and the GSC. Panels **A. - C.** show the results for the western GSC and panels **D. - F.** show the results for the eastern GSC. Panels **A.** and **D.** show the input parameters for these models (i.e. the fraction of channelised melt), and the geochemical (**B.** and **E.**) and crustal thickness (**C.** and **F.**) results are shown below. Crustal thickness estimates are from Ito and Lin (1995; red), Canales et al. (2002; blue), and Mittelstaedt et al. (2014; black); modelled crustal thickness is shown in blue (solid line). It can be observed that, by assuming channelised flow occurs beneath the volcanic lineaments of the Northern Galápagos Volcanic Province, the crustal thickness and geochemical signature of the basalts from the western GSC are more accurately reproduced in this model than in the model of solid-state plume-ridge interaction shown in Fig. 4.

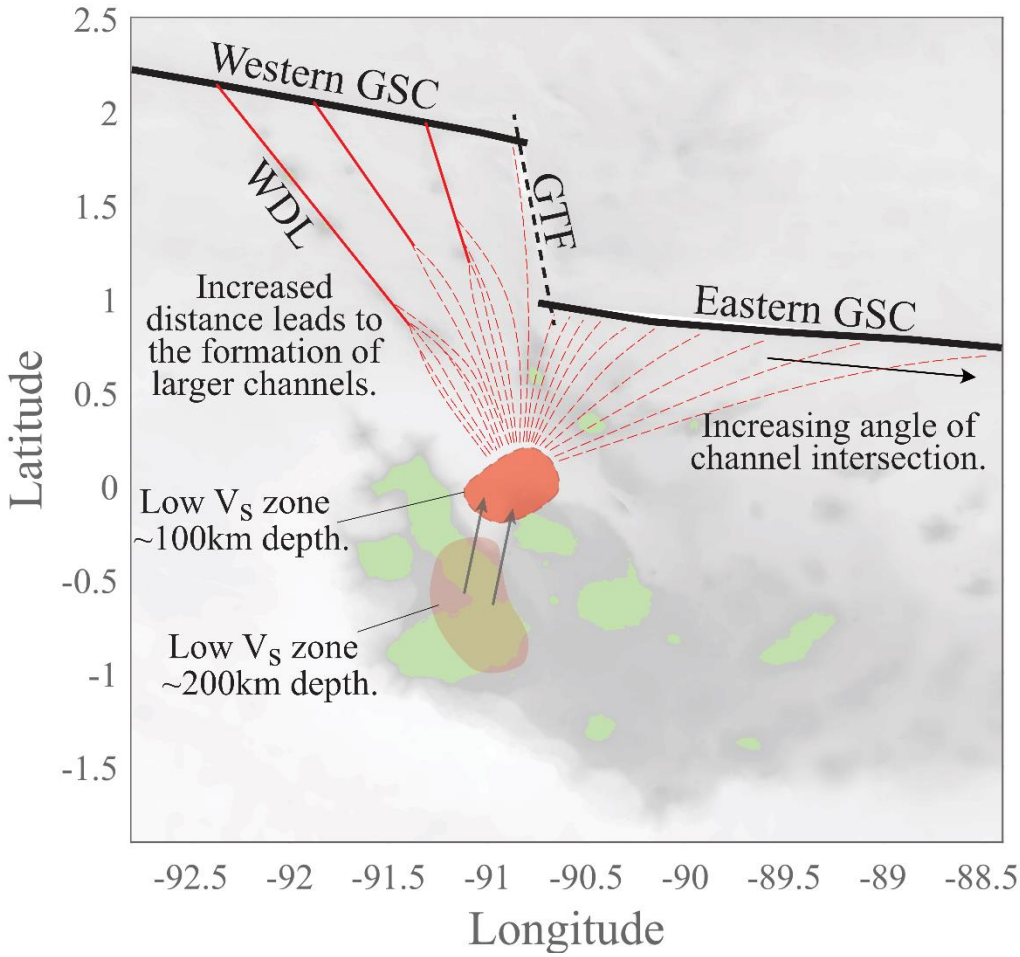

1218

1219 **Figure 6 –** Schematic diagram illustrating the nature of the melt channels beneath the northern
1220 Galápagos volcanic province. The eastern GSC is fed by a large number of small melt channels and
1221 the influence of these melt channels declines with increasing distance to the mantle plume. On the
1222 western GSC our models predict that the melt channels amalgamate into three larger channels that
1223 are located beneath each of the three volcanic lineaments in the northern Galápagos volcanic
1224 province. The location of the Galápagos mantle plume at depths of 200 and 100 km is taken from
1225 Villagómez et al. (2014).

1226

1227

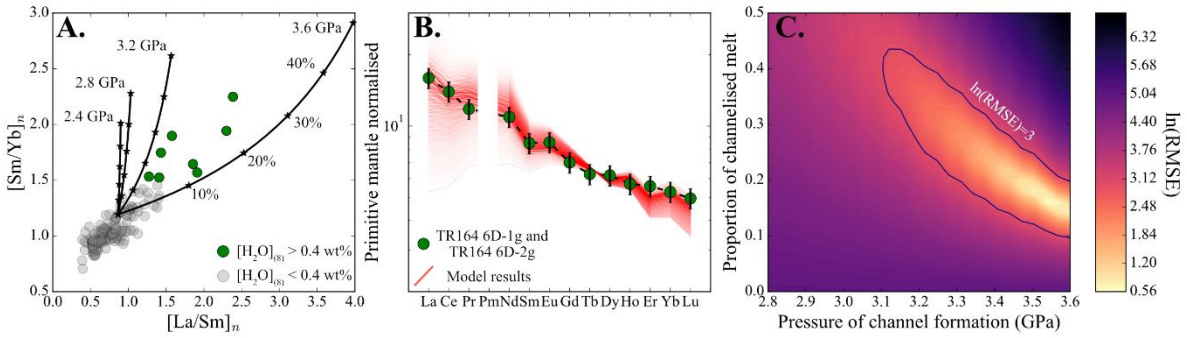

Figure 7 – Comparison of our mantle melting models that include a contribution of plume-derived channelised melts to the composition of the anomalously enriched basalts from the GSC. **A.** composition of basalts that cannot be reproduced by our along-ridge models of plume-ridge interaction are shown in green and are generally characterised by $[H_2O]_{(8)}$ contents above 0.4 wt%. The composition of these enriched basalts is best reproduced when the proportion of channelised melt is >15% and the depth of channel formation is >3.2 GPa. Notably, as the pymelt simulations do not account for the presence of H_2O on the pyroxenite solidus, parameterisation of hydrous melting might influence our estimates for the pressure of channel formation. **B.** Comparison of 676 models to the composition of the TR164 6D-1g and TR164 6D-2g basalts (89.59 °W). The models with the lowest RMSE are shown by the darker colours. **C.** RMSE for all models shown in **B.** where the contribution of channelised melt is between 0 and 50%, and the pressure of channel formation is between 2.8 and 3.6 GPa. In all models the composition of the channelised melts are calculated using a T_P of 1400 °C and a pyroxenite source fraction of 20% (Gleeson et al. 2021).

Scenario 1: anomalously high delivery of channelised melt leads to crustal thickness anomaly.

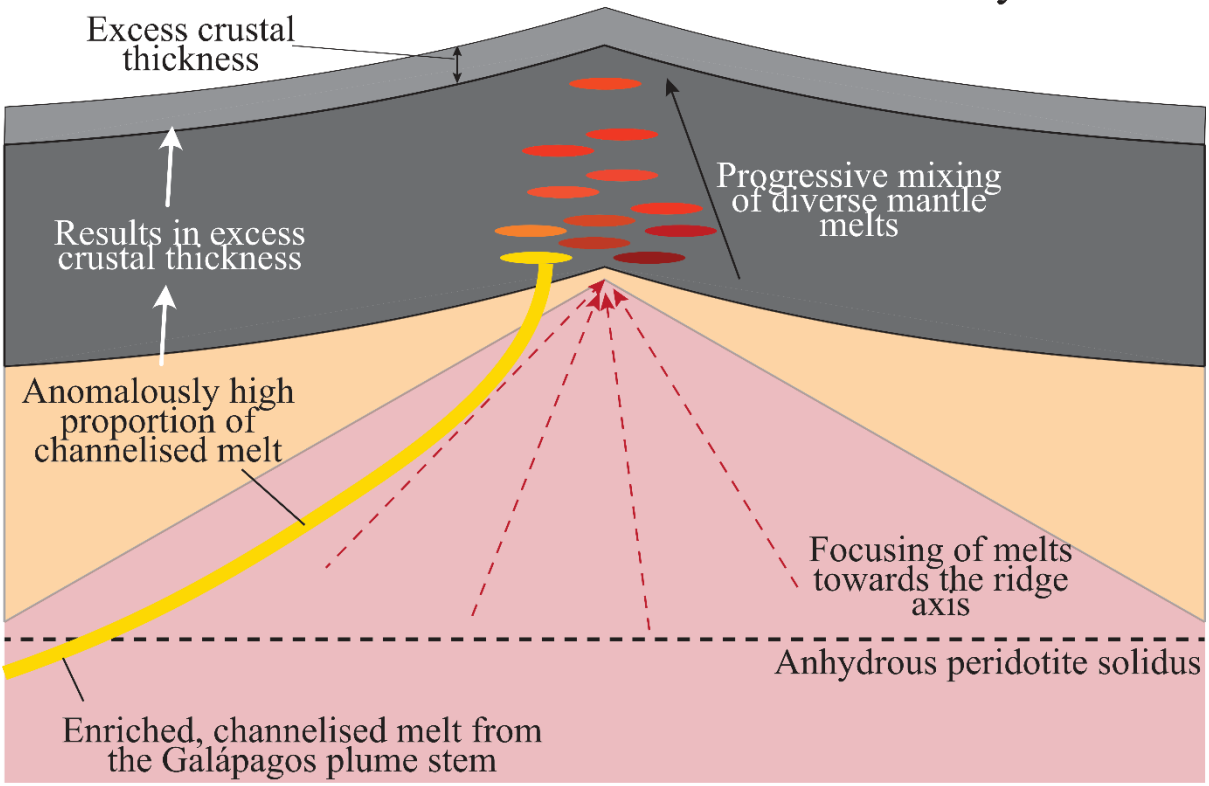

Scenario 2: Melts derived from the Galapagos plume stem incompletely mix with melts formed beneath the ridge axis.

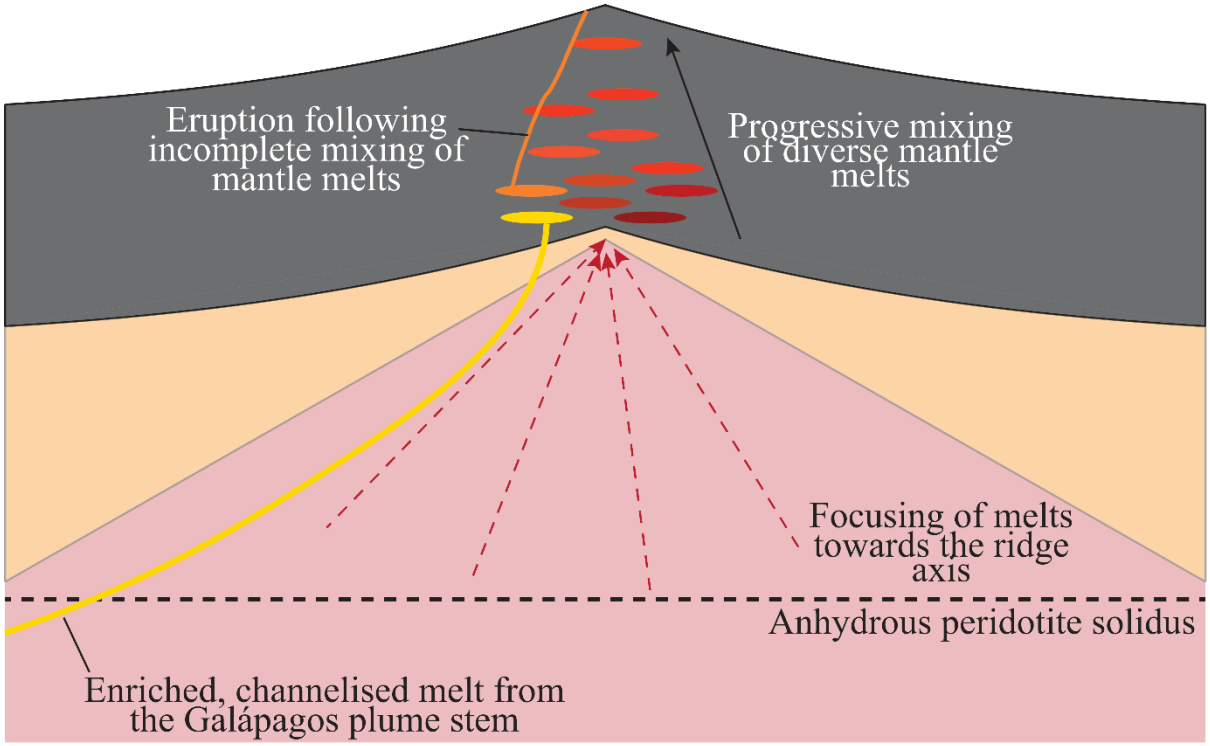

Figure 8 – Schematic diagram displaying the two ways in which delivery of channelised melt might contribute to the geochemical and geophysical parameters (such as crustal thickness) observed along the GSC. In Scenario 1, an anomalously high flux of channelised melt to the GSC results in moderately-to-highly enriched basalts at the surface and anomalously thick crust (e.g. at the intersection of the WDL with the GSC). In scenario 2, only a moderate supply of channelised melt exists. However, some of this channelised melt manages to ascend and erupt without completely mixing and/or homogenising with melts formed beneath the ridge axis leading to the presence of anomalously enriched basalts at the surface.

1251

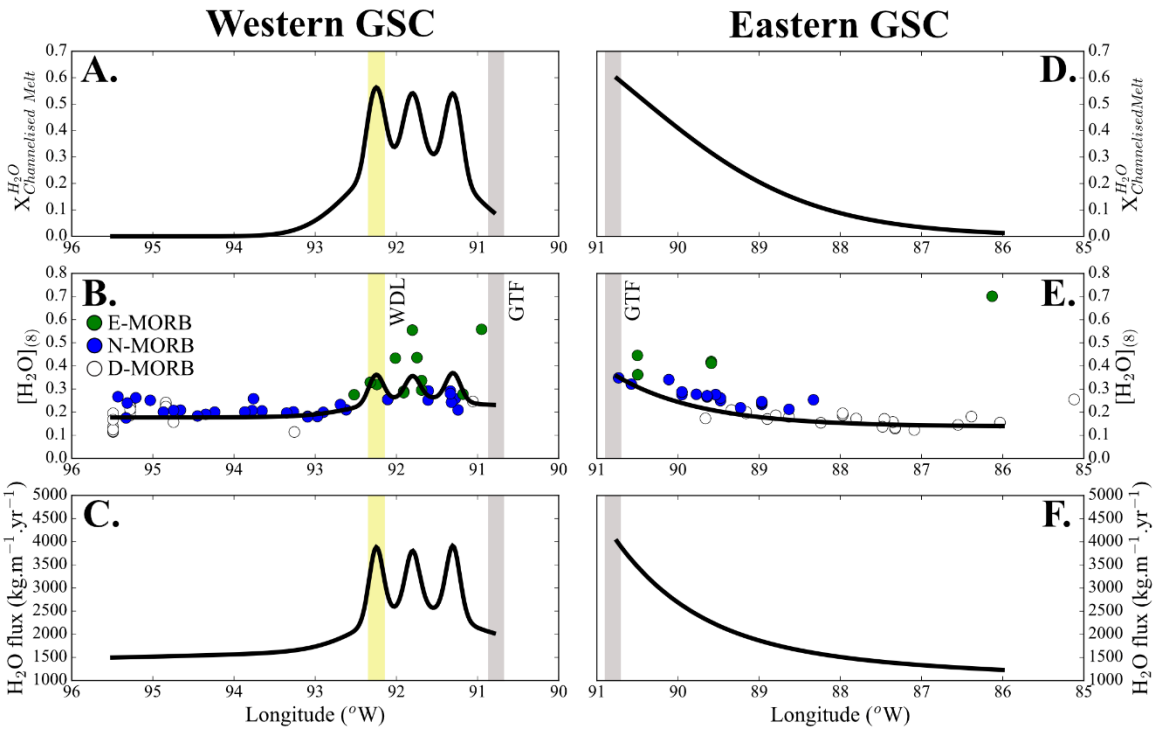

1252

1253 **Figure 9 –** H_2O concentrations and fluxes predicted by new models of plume-ridge interaction in the

1254 Galápagos (models are identical to those shown in Fig. 5). The model accurately recreates the H_2O

1255 contents of basalts from both the eastern GSC and the western GSC (model results assume ~20%

1256 fractionation of olivine and/or plagioclase). The maximum outflux of H_2O along the western GSC is

1257 ~4000 $kg.m^{-1}.yr^{-1}$ where the volcanic lineaments intersect the GSC (compared to the background flux

1258 of only ~2000 $kg.m^{-1}.yr^{-1}$). The greatest outflux of H_2O from the GSC is observed on the eastern GSC

1259 near the GTF (~4000 $kg.m^{-1}.yr^{-1}$) and, in this location, ~60% of the H_2O flux out of the GSC is sourced

1260 from plume-derived channelized melts.

Table 1 – Parameters used in the solid-state and melt channelisation models of plume-ridge interaction (shown in Figures 4 and 5, respectively).

	Solid State models		Melt channelisation models	
Parameter	Western GSC	Eastern GSC	Western GSC	Eastern GSC
T_p at GTF (°C)	1370	1375	1372	1387
T_p distal from GTF (°C)	1360	1365	1362	1365
$U_{r\text{-}max}$ at GTF	7	8	2.5	1.8
A[a]	0.6	0.5	0.6	0.4
B[a]	6	8	1.5	0.8
C[a]	0	0	0	0
X_{Pyx}	0.10	0.10	0.06	0.08
A	0.4	0.4	0.4	0.3
B	0.08	0.09	0.04	0.06
C	0.02	0.01	0.02	0.02
$P_{termination}$ (GPa)[b] at GTF	0.65	0.7	0.43	0.6
A	1.5	1.5	1.5	1.2
B	0.40	0.45	0.18	0.35
C	0.25	0.25	0.25	0.25
H_2O (peridotite)	145	100	145	100
H_2O (pyroxenite)	550	550	550	550
T_p for generation of channelised melts	n/a	n/a	1400	1400

[a] $U_{r\text{-}max}$, X_{Pyx}, and $P_{termination}$ are calculated according to $(U_{r-max}, X_{Pyx}, P_{termination}) = \exp\left(-\left((Long(°W) - 90.8) \times A\right)\right) \times B + C$ on the western GSC and $(U_{r-max}, X_{Pyx}, P_{termination}) = \exp\left(-\left(\left(90.8 - Long(°W)\right) \times A\right)\right) \times B$+C on the eastern GSC.

[b] $P_{termination}$ (GPa) refers to the pressure at the top of the melt column.